Ore Geology Reviews 65 (2015) 55–69

Contents lists available at ScienceDirect

Ore Geology Reviews

journal homepage: www.elsevier.com/locate/oregeorev

# Infrared microthermometric and noble gas isotope study of fluid inclusions in ore minerals at the Woxi orogenic Au–Sb–W deposit, western Hunan, South China

Ya-Nan Zhu [a,b], Jian-Tang Peng [a,c,*]

[a] State Key Laboratory of Ore Deposit Geochemistry, Institute of Geochemistry, Chinese Academy of Sciences, Guiyang 550002, PR China
[b] University of Chinese Academy of Sciences, Beijing 100049, PR China
[c] Key Laboratory of Metallogenic Prediction of Nonferrous Metals, Ministry of Education, School of Geosciences and Info-physics, Central South University, Changsha 410083, PR China

ARTICLE INFO

*Article history:*
Received 2 March 2014
Received in revised form 11 August 2014
Accepted 12 August 2014
Available online 16 September 2014

*Keywords:*
Fluid inclusions
Noble gas isotope
Ore minerals
Orogenic Au–Sb–W deposit

ABSTRACT

The Woxi Au–Sb–W deposit, hosted by the Neoproterozoic low-grade metamorphic clastic rocks, is located in a brittle-ductile shear zone within the Xuefengshan Range, South China. Orebodies are predominantly banded quartz veins, which are strictly controlled by bedding faults and display significant vertical extents (up to 2 km) without obvious vertical metal zoning. Fluid inclusions hosted in quartz, scheelite, and stibnite from quartz–scheelite and quartz–sulfide–gold veins have been studied using conventional and infrared microscopy, respectively. Four types of fluid inclusions were identified based on petrography, including type I (two-phase, liquid-rich aqueous inclusions), type II (two- or three-phase, $CO_2$-rich inclusions), type III (two-phase, vapour-rich aqueous inclusions), and type IV (single-phase aqueous inclusions). The fluid inclusions in ore minerals (scheelite and stibnite) and their coexisting quartz largely share similar characteristics in terms of their types, homogenization temperatures and salinities. This is consistent with the fact that these ore minerals are always intergrown with quartz. Microthermometric and laser Raman data indicate a low-to-moderate temperature (140–240 °C), low salinity (<7.0 wt.% NaCl equiv.), $CO_2$-rich, $N_2$-bearing aqueous ore-forming fluid. Such fluid is further identified as a deeply non-magmatic crustal fluid rather than a mantle-source fluid by the significantly low $^3He/^4He$ ratios (0.002–0.281 Ra), and a small amount of meteoric water or host-rock-buffered fluid could be involved. W ore precipitation was probably associated with mixing between a deeply-originated crustal fluid and host-rock-buffered fluid based on the fluid inclusion features in scheelite and quartz-I. However, Au and Sb ore deposition probably resulted from boiling which was caused by the marked pressure drop. Geological features (such as banded structure and crack-sealing structure) also indicate that fluid pressure fluctuation induced by fault-valve mechanism occurred during ore precipitation. These characteristics of the ore-forming fluids in the Woxi deposit are in good agreement with the definition of orogenic gold deposits and the Woxi Au–Sb–W deposit is probably an atypical orogenic gold deposit for its unique ore-forming element association.


## 1. Introduction

The physico-chemical properties of fluids and solids trapped in ore minerals and coeval gangue minerals provide key information about controls on metal deposition in ore deposits. Although a few metallic minerals such as scheelite and some sphalerite are transparent, most are opaque under the traditional transmitted-light microscope. Thus, in the past several decades, fluid inclusions were usually studied only within transparent gangue minerals, and their microthermometric data were extrapolated to the coexisting ore minerals. With the application of infrared microscopy in earth sciences in recent years, fluid inclusions in some opaque ore minerals, e.g. wolframite (Bailly et al., 2002; Campbell et al., 1984; Lüders, 1996; Wei et al., 2012), stibnite (Bailly et al., 2000; Buchholz et al., 2007; Hagemann and Lüders, 2003; Lüders, 1996), and pyrite (Kouzmanov et al., 2010; Lindaas et al., 2002; Lüders and Ziemann, 1999; Zhu et al., 2013), can be directly observed and analysed, revealing that different homogenization temperatures and salinities probably exist between the spatially associated gangue and ore minerals in some hydrothermal deposits (e.g. Bailly et al., 2000; Campbell and Panter, 1990; Wang et al., 2013; Wei et al., 2012), even for those documented cases where unambiguous textural evidence demonstrates a clear coeval timing between gangue and ore minerals (Campbell and Robinson-Cook, 1987; Giamello et al., 1992). Thus, examining fluid inclusions in ore minerals is crucial; it can

* Corresponding author at: State Key Laboratory of Ore Deposit Geochemistry, Institute of Geochemistry, Chinese Academy of Sciences, Guiyang 550002, PR China.
*E-mail address:* jtpeng@126.com (J.-T. Peng).

http://dx.doi.org/10.1016/j.oregeorev.2014.08.014
0169-1368/

preclude any doubt whether fluid inclusions studied in gangue minerals adequately reflect the ore-forming fluids from which ore minerals precipitated.

Gold-only lode deposits are genetically associated with low salinity (typically <6 wt.% NaCl equiv.) aqueous, $CO_2$-bearing fluid inclusions similar to fluids generated during transitional sub-greenschist to amphibolite facies metamorphism of altered volcanosedimentary rocks (Goldfarb et al., 2005; Groves et al., 1998; Kerrich et al., 2000; Tomkins, 2013). These deposits are found from the Archean to recent orogenic belts (Chen et al., 2012a; de Boorder, 2012; Goldfarb et al., 2001; Hronsky et al., 2012; Zachariáš et al., 2013), and considered to be an inherent part of an orogeny (Fu et al., 2012; Groves et al., 2005). Lode gold deposits are widespread in the Precambrian low-grade metamorphic clastic rocks throughout the Xuefengshan Range, western Hunan, South China, and are also considered to be orogenic deposits (Chen, 2006; Zhou et al., 2002). However, compared to typical orogenic "gold-only" ore deposits, the ore-forming element associations for these gold deposits are unique, predominated by Au–Sb–W, Au–W, and Au–Sb. As the largest gold deposit occurred in the Xuefengshan Range, the Woxi Au–Sb–W deposit is representative of these unique metal association gold deposits in this region, it provides an important natural laboratory for investigating the nature and source of ore-forming fluid of lode gold deposits in the Xuefengshan Range.

Few systematic fluid inclusion studies on ore minerals (especially opaque ore minerals) have been performed on the Woxi Au–Sb–W deposit, although many genetic opinions have been proposed for this deposit, including (1) sedimentary exhalative (SEDEX) origin (Gu et al., 2007, 2012; Zhang, 1985), (2) magmatic hydrothermal origin (Mao and Li, 1997; Peng and Frei, 2004), and (3) metamorphic hydrothermal origin (Luo et al., 1984; Yang, 1992). In this study, fluid inclusions hosted in scheelite and stibnite, as the most important ore minerals in different ore-forming stages, are examined. For comparison, fluid inclusions in their coexisting quartz are also studied. In addition, noble gas isotope data on ore minerals are determined, for the purpose of tracing possible fluid sources and mineralization processes of the ore-forming fluids (e.g. Burgess et al., 1992; Kendrick et al., 2011; Landis and Hofstra, 2012; Li et al., 2011; Zeng et al., 2014). The objectives of this paper are: (1) to decipher the nature and sources of the fluids involved in the formation of gold, antimony and tungsten ores in the Woxi deposit; (2) to determine the characteristics of the hydrothermal fluids responsible for gold, stibnite, and/or scheelite deposition in the Xuefengshan Range on the basis of fluid inclusion data obtained in this study and previous studies; and (3) to give some new genetic constraints for the Woxi deposit.

## 2. Regional geology

The Xuefengshan Range in western Hunan, South China, is located between the Yangtze Block and the Cathaysia Block (Fig. 1). It consists mainly of the Mesoproterozoic Lengjiaxi Group and Neoproterozoic Banxi Group (HBGMR, 1988). The Lengjiaxi Group is composed of flysch-type sedimentary rocks, including marine clastic rocks intercalated with lava flows. The Banxi Group consists of flyschoid-type clastic rocks and argillite. All the Proterozoic strata were extensively deformed and metamorphosed to sub-greenschist facies during regional metamorphism at ~1000 and ~800 Ma (HBGMR, 1988). The cover sequence includes Sinian and Cambrian strata, with minor Ordovician and Silurian strata. Recent studies suggest that the Xuefengshan Range was involved in the early Paleozoic and early Mesozoic intracontinental orogens, recorded by magmatism, folding, faulting and metamorphic deformation (Chu et al., 2012; Li et al., 2009; Zhang et al., 2013). In addition, compared to the eastern Xuefengshan Range, magmatic activity in the western part is relatively scarce.

Lode gold deposits are widespread throughout the Xuefengshan Range. Gold mineralization usually occurs in the Proterozoic, Sinian and Cambrian low-grade metamorphic clastic rocks, and has metal

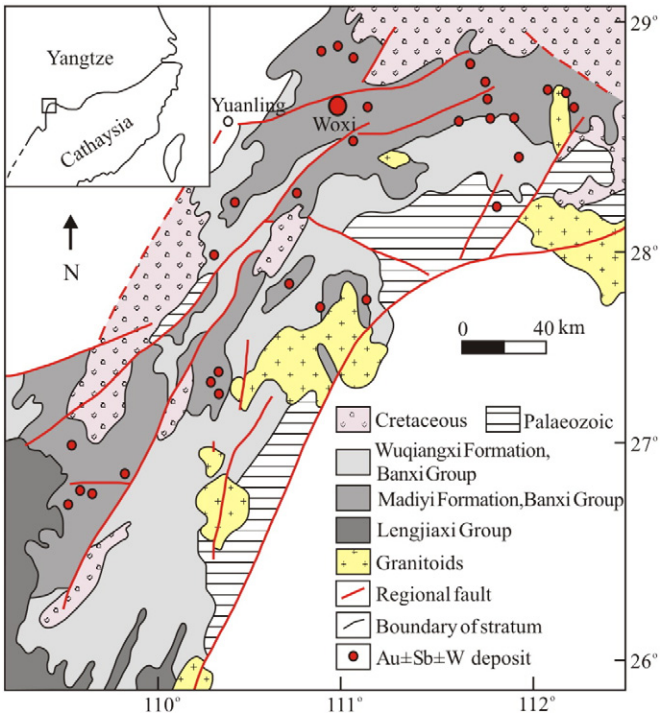


**Fig. 1.** Geological sketch map of the Xuefengshan Range in western Hunan, China (modified after Peng and Frei, 2004).

associations of Au–(Sb–W). For example, the Woxi Au–Sb–W deposit (Peng and Frei, 2004; Peng et al., 2003a), the Fuzhuxi and Xichong Au–Sb deposits (Yao and Zhu, 1993), the Xi'an Au–W deposit, and the Mobin and Herenping Au deposits. The Woxi deposit is the largest gold deposit in the Xuefengshan Range and displays a unique Au–Sb–W metal association.

## 3. Ore deposit geology

The Woxi Au–Sb–W deposit is located in the Xuefengshan Range in western Hunan, South China (Fig. 1). It was discovered in 1875, and mining began in 1895. The Au, Sb, and $WO_3$ metal reserves for the Woxi deposit amount to >50, 220,000, and 25,000 t, and the average grades of Au, Sb, and W in the ores are 9.77 ppm, 2.84%, and 0.3%, respectively. In general, the metal minerals display an obvious lateral zoning, ranging from W–Au in the east, to W–Sb–Au in the middle, and Sb–Au in the west, accompanying tungsten mineral phase from scheelite to wolframite (GHCPAPF, 1996).

The strata exposed in the Woxi region mainly consist of the Proterozoic Lengjiaxi Group and Banxi Group (Fig. 2). The latter, which is a series of flyschoid consisting of slate and phyllite interbedded with local volcanic materials, can be subdivided into the Madiyi Formation and the Wuqiangxi Formation. The Wuqiangxi Formation concordantly overlies the Madiyi Formation, and the latter discordantly overlies the Lengjiaxi Group (Luo et al., 1984). The lithologic sequence of the Madiyi Formation consists of low-grade metamorphic purple-red sericite slate, sandstone slate, and calcareous sericitic slate; orebodies in this deposit are restricted within the purple-red calcareous sericitic slate in the middle Madiyi Formation, and controlled by interlay faults (Fig. 2A–B). No magmatic activities are preserved in the mining district or adjacent regions (Fig. 2A).

Orebodies in the Woxi mining district are predominantly composed of quartz veins, which occur in the footwall of the E–W striking Woxi Fault (GHCPAPF, 1996). These quartz veins can be divided into banded vein, network vein (or veinlet), and discordant vein (e.g. Fig. 3A–C; Luo et al., 1984; Gu et al., 2007). Economically, the banded veins rank as the most important, contributing about 70% of the metal

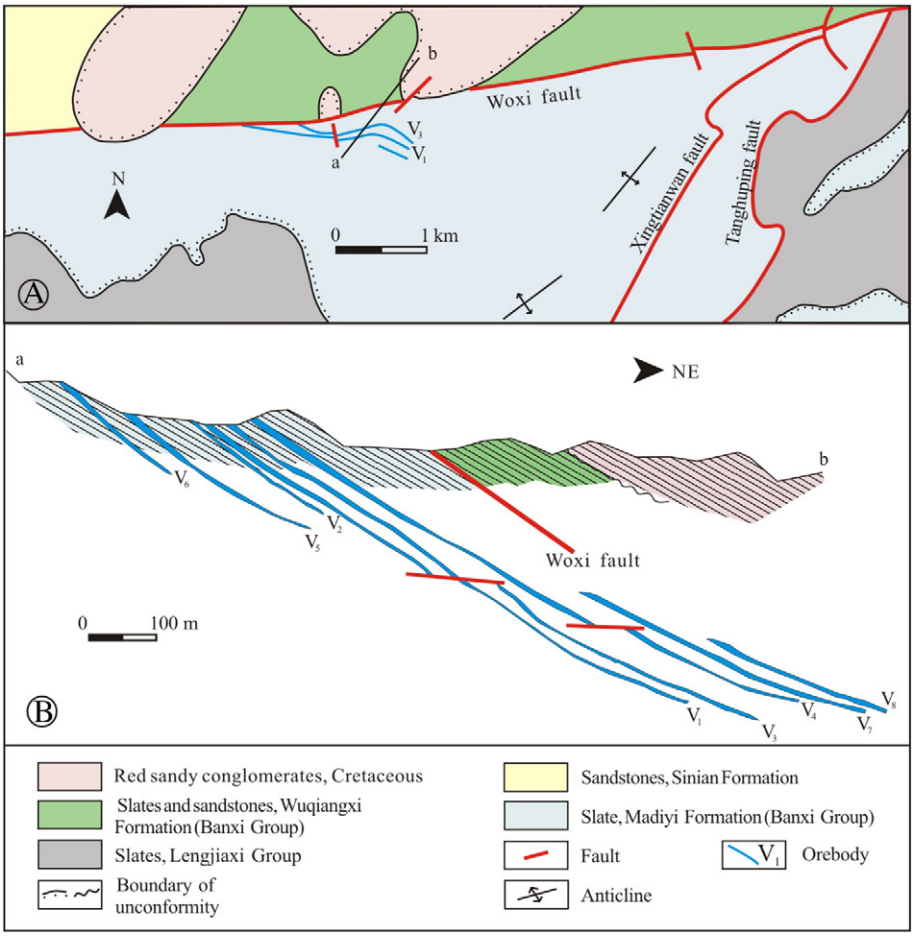


**Fig. 2.** Sketch map of the Woxi deposit district (modified after GHCPAPF, 1996). (A) Geological map; (B) Cross section a-b (marked in A) through the Woxi deposit.

accumulations for this deposit (Luo et al., 1984). They are E–W striking, gentle dipping (~20°–30°), with significant vertical extents (up to 2 km) and without obvious vertical metal zoning.

These gently-dipping veins are commonly parallel to the host strata and the Woxi Fault (Fig. 2B), and display open-space filling textures (Fig. 3D–E), containing brecciated vein fragments (Fig. 3D) or wall rocks (Fig. 3E). Boudinage and folding of some veins are also observed (Fig. 3F; Li et al., 1983; Liu, 1992), reflecting their pre-kinematic to, more commonly, syn-kinematic timing. The alteration halo around these ore veins in clastic sedimentary rocks is distinguished as widespread silicification, pyritization, carbonatization and sericitization.

Metallic minerals are dominated by scheelite (Fig. 4A), pyrite (Fig. 4B–E), stibnite (Fig. 4C–F), native gold (Fig. 4G–H) and locally wolframite, with minor arsenopyrite, sphalerite, and galena; the gangue minerals include quartz (Fig. 4A–H) and minor amounts of sericite, carbonate, and chlorite (GHCPAPF, 1996). Detailed mineralogical features have been previously documented (GHCPAPF, 1996; Liang and Zhang, 1986; Shao et al., 1996; Zhang et al., 1996) and the mineral paragenesis for the Woxi deposit was divided into the quartz–carbonate stage, quartz–scheelite stage, quartz–sulfide–gold stage, and quartz–carbonate stage (GHCPAPF, 1996; Liang et al., 1981; Liu, 1992). Features of each stage are summarized in Fig. 5.

The early quartz–carbonate stage is barren with no discernible wall rock alteration zones present (GHCPAPF, 1996).

The quartz–scheelite stage consists mainly of massive quartz (Fig. 4A, C) with scheelite (Fig. 4A), wolframite, carbonate, apatite, minor arsenopyrite and siderite. Wolframite is less abundant than scheelite and usually occurs in the western mining area (GHCPAPF, 1996; Zhu et al., 2014). Scheelite occurs as irregularly shaped and massive aggregates in quartz veins, commonly cut by the later quartz veinlets containing pyrite, stibnite, or native gold (Fig. 4A). Quartz, the most abundant mineral, mainly appears as subhedral–anhedral grains and is commonly brecciated (Fig. 4A, C, D, E).

The quartz–sulfide–gold stage is characterized by the widespread occurrence of pyrite (Fig. 4B–E), stibnite (Fig. 4C–E), and native gold (Fig. 4G–H), with minor arsenopyrite, sphalerite, galena, and sulfosalt minerals. The earlier quartz–scheelite ore fragments sometimes occur in the quartz–sulfide–gold veins (Fig. 3D, 4D–4E). Pyrite is the most abundant gold-bearing mineral in these veins, followed by stibnite, scheelite, and quartz (GHCPAPF, 1996). Pyrite appears as euhedral–subhedral grains with variable size, and mainly occurs as banded veins, disseminated grains, and veinlets in the massive quartz or the altered host rocks (Fig. 4A–E). Native gold is locally present along the boundaries or in the fissures of pyrite grains (Fig. 4H). Stibnite is irregular in shape and is present in the quartz veins as isolated grains or as euhedral–anhedral massive aggregates, commonly coexisting with fine quartz and pyrite (Fig. 4C–F).

The later quartz–carbonate stage is marked by the appearance of carbonate and quartz with trace amounts of native gold and pyrite (GHCPAPF, 1996). These minerals fill the fissures in early veins, or occur in the vugs.

## 4. Samples and analytical methods

### 4.1. Fluid inclusions

All samples in this study were collected from underground exposures. Fluid inclusions were examined in scheelite and coexisting quartz

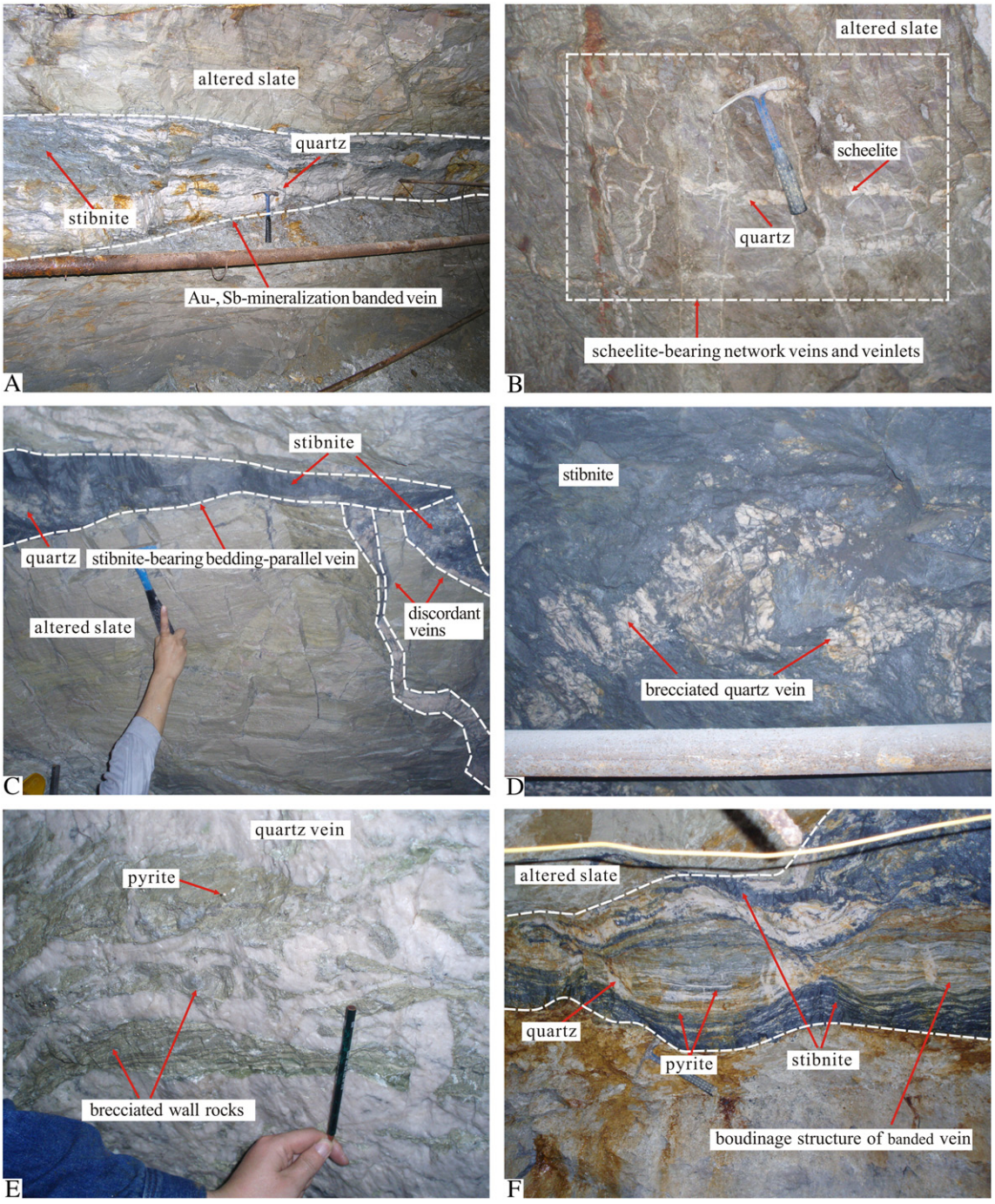


**Fig. 3.** Occurrences of ore veins in the Woxi deposit. (A) Bedding-parallel banded Au- and Sb-mineralization vein. (B) Quartz–scheelite veinlets intersected at nearly right angles. (C) A pinch-out bedding-parallel vein and two discordant veins. (D) Brecciated quartz vein in massive stibnite. (E) Brecciated host rocks in quartz vein. (F) Boudinage of banded stibnite–gold–quartz vein.

(quartz-I; e.g. Fig. 4A) from the quartz–scheelite veins, and in stibnite and coexisting quartz (quartz-II; e.g. Fig. 4D, F) from the quartz–sulfide–gold veins. Microthermometric measurements of fluid inclusions in stibnite were carried out on a heating–freezing system mounted on an Olympus BH51 infrared microscope. To minimize the effects of the infrared light intensity on the salinity and homogenization temperature of the fluid inclusions in opaque minerals, microthermometric analyses were carried out carefully with the lowest possible light intensity, and with all possible diaphragms nearly closed (Moritz, 2006). Fluid inclusions in scheelite and quartz were measured by a Linkam THMSG 600 programmable heating–freezing stage mounted on a Leica microscope, calibrated with melting-point standards ($CCl_4$, −22.99 °C; $KNO_3$,

**Fig. 4.** Photographs of hand specimen samples and photomicrographs of ore and gangue minerals from the Woxi deposit. (A) Crack-sealing structure. Pyrite and quartz-II filled in the fracture of scheelite-quartz vein. (B) Banded vein. The band is composed of pyrite precipitated during successive hydraulic fracturing events. (C) Banded veins. The bands are composed of pyrite or stibnite or altered slate fragment. (D) Brecciated quartz vein in massive stibnite. (E) Mesh-vein structure. Pyrite and stibnite formed in the mesh fissures of early stage veins. (F) Euhedral fine-grained quartz-II in stibnite. (G) Native gold disseminated in the quartz vein. (H) Native gold occurs along the boundary of pyrite grains. A, D and E reflect the reopening of the early stage veins. Abbreviations for minerals are Py: pyrite; Sch: scheelite; Qz: quartz; St: stibnite.

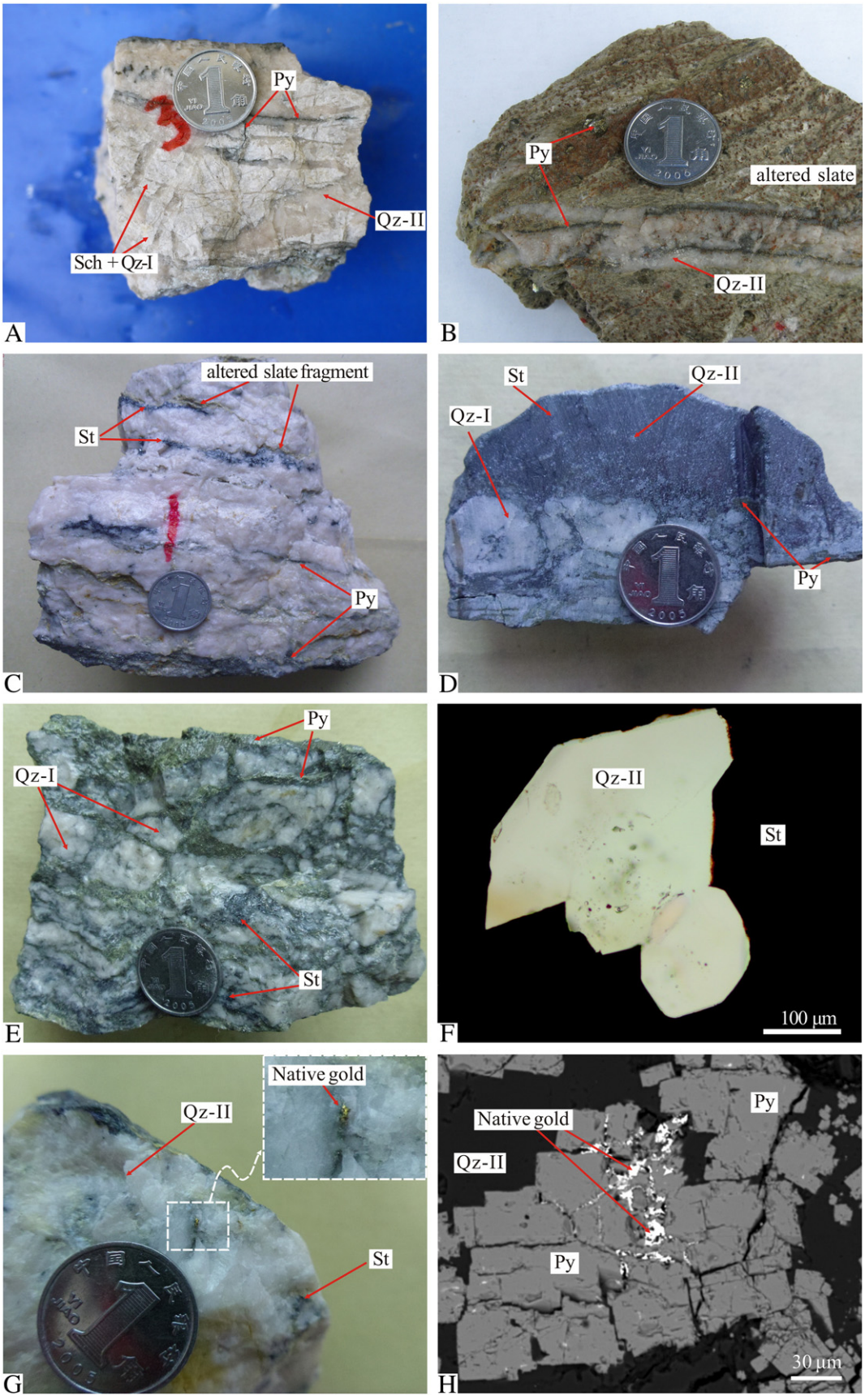
Py
Qz-II
Sch + Qz-I
A
Py
altered slate
Qz-II
B
altered slate fragment
St
Py
C
St
Qz-II
Qz-I
Py
D
Py
Qz-I
St
E
Qz-II
St
100 μm
F
Native gold
Qz-II
St
G
Py
Native gold
Qz-II
Py
30 μm
H

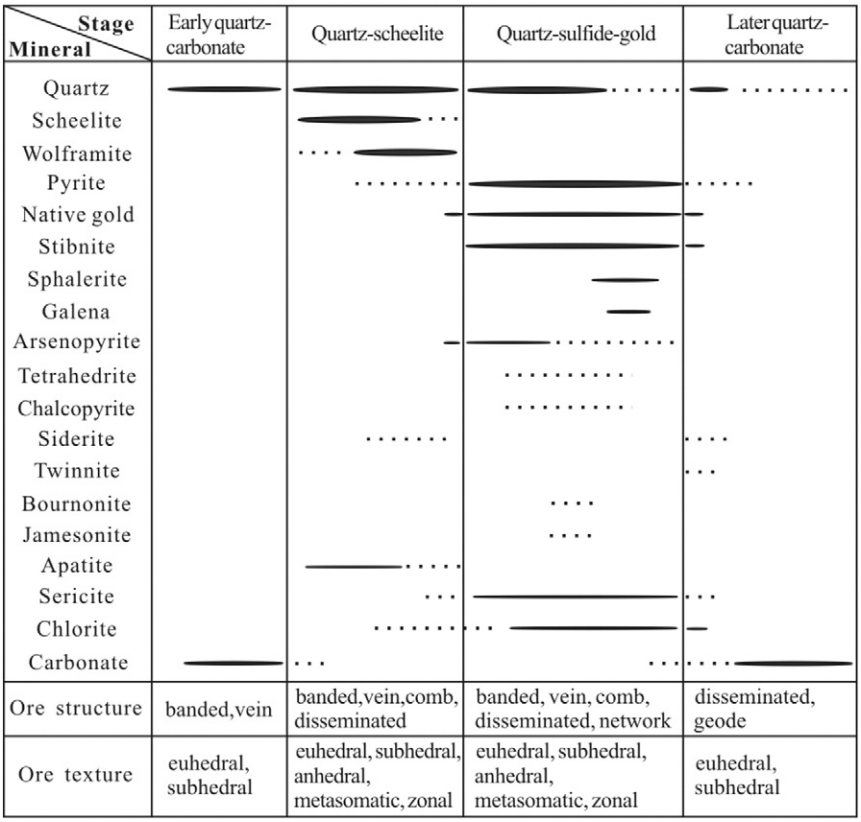


**Fig. 5.** Paragenetic sequence of minerals from the Woxi deposit (modified after GHCPAPF, 1996).

333 °C) and the melting point of $CO_2$ (−56.6 °C) in synthetic fluid inclusions. The uncertainty of temperature measurements in this study was approximately ±0.2 °C below 50 °C and ±2 °C above 100 °C. A heating rate of 0.1 °C/min is adopted near the melting temperatures of carbonic phase, clathrate, and ice. Compositions of individual fluid inclusion in quartz and scheelite, including vapour and liquid, were identified by using laser Raman spectroscopy. All of these above experiments were performed at the State Key Laboratory of Ore Deposit Geochemistry, Institute of Geochemistry, Chinese Academy of Sciences.

Salinities of two-phase aqueous inclusions and $CO_2$-rich inclusions were respectively calculated from the final melting temperature of ice or clathrate following the method proposed by Bodnar (1993) and Lu et al. (2004). Bulk composition and density of aqueous and carbonic phases of the two-phase aqueous inclusions were calculated by using the online calculation (gcmodel.kl-edi.ac.cn/archives/), whereas those of the $CO_2$-rich inclusions were determined with the MacFlinCor Program (Brown and Lamb, 1989).

### 4.2. Noble gas isotope

Fresh pyrite and stibnite samples have been collected from the quartz–sulfide–gold veins and their adjacent alteration wall rocks of the Woxi deposit. Noble gas compositions of the fluid inclusions hosted in these samples were released by stepwise heating, which is a powerful and widely adopted technique in noble gas analysis (Bruno et al., 1997; Hou et al., 2011; Kendrick et al., 2001; Rai et al., 2003; Reynolds et al., 1970; Wieler et al., 1986). Pyrite appears to be one of the best preservers for noble gases (Ballentine et al., 2002; Burnard et al., 1999; Hu et al., 1998; Stuart et al., 1994). Due to extremely low concentration of U, Th and K in sulfide, in situ additions of radiogenic $^4He$ and $^{40}Ar$ in pyrite and stibnite are likely to be negligible. The effect of cosmogenic nuclides can also be ignored because all samples were collected from underground exposures. After these samples were crushed, mineral separates were handpicked under a binocular microscope. The concentrations and isotopic compositions of noble gases were measured using a MM5400 mass spectrometer at the Key Laboratory of Petroleum Resources Research (Lanzhou), Institute of Geology and Geophysics, Chinese Academy of Sciences. The analytical procedures adopted in this study have been described in detail by Ye et al. (2007).

## 5. Fluid inclusion petrography

Representative samples of scheelite, stibnite, and their corresponding coexisting quartz were selected for fluid inclusion analysis. The quantity and quality of fluid inclusions were relatively variable. The criteria proposed by Roedder (1984) were used to discriminate among primary, pseudosecondary and secondary fluid inclusions. Measurements in this study were only performed on those inclusions considered as primary or pseudosecondary (e.g. Figs. 6–7). These inclusions are mainly classified into four types at room temperature on the basis of phases, phase proportions, and composition: type I (two-phase, liquid-rich aqueous inclusions), type II (type IIa: two-phase $CO_2$-rich inclusions, and type IIb: three-phase $CO_2$-rich inclusions), type III (two-phase, vapour-rich aqueous inclusions), and type IV (single-phase aqueous inclusions).

Type I inclusions are the most abundant in all minerals, with the vapour phase ranging from 5% to 45% of the total volume of the inclusions at room temperature. They are negative crystal, elliptical, flat, tubular, or irregular in shape, from a few microns to 20 μm (>50 μm in stibnite) in size, and occur isolated or in groups (Figs. 6A, B, D and E; 7A, B, E, F and H).

Type II inclusions, have not been reported in previous studies (Ding et al., 1981; Dong et al., 2008; Niu and Ma, 1991), but are relatively common in the samples examined in this present study. Large quantities of type II inclusions are observed in scheelite (Fig. 6F) and quartz-II (Fig. 7A, C and D) samples, lesser quantities exist in quartz-I (Fig. 6C), and few are present in stibnite (Fig. 7I). The $CO_2$ phase of type II inclusions can occupy 15%–90% of the inclusion volumes at room

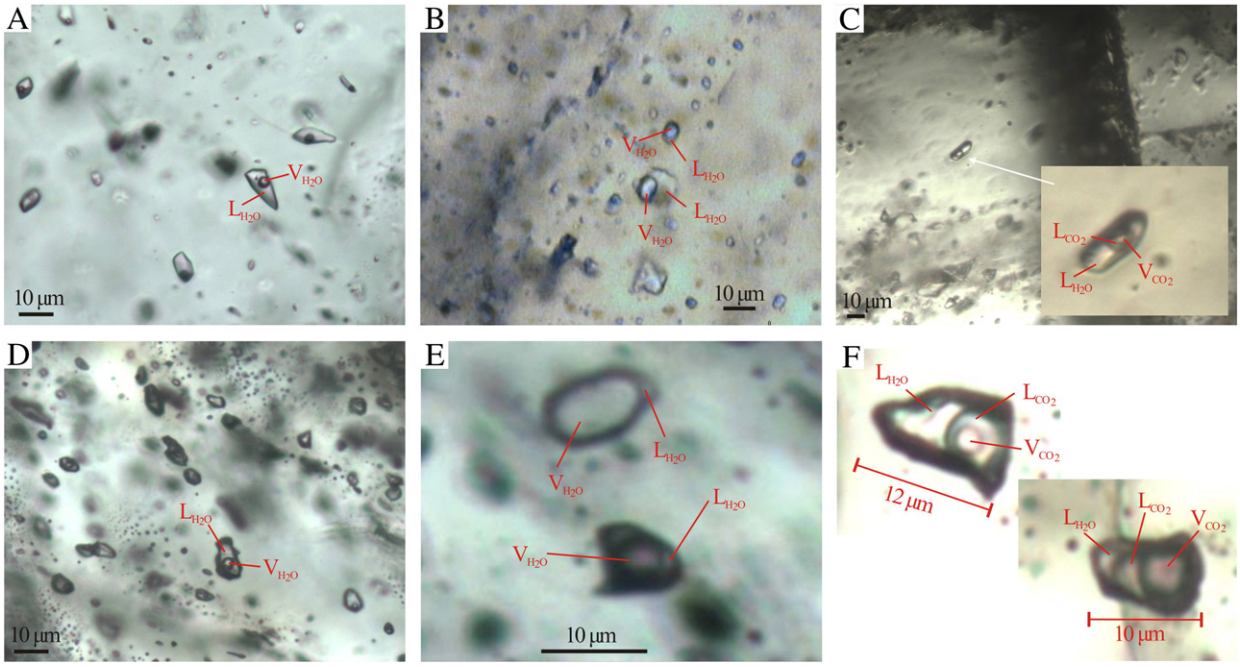


**Fig. 6.** Photomicrographs of representative fluid inclusion types at room temperature in quartz–scheelite stage. (A) Type I inclusions in quartz-I. (B) Coexistence of type I and type III inclusions in quartz-I. (C) Type II inclusions containing a vapour $CO_2$ and a liquid $CO_2$ and $H_2O$ phase in quartz-I. (D) Type I inclusions in scheelite. (E) Coexistence of type I and type III inclusions in scheelite. (F) Type II inclusions in scheelite.

temperature (e.g. Figs. 6F and 7C). These inclusions mainly occur isolated or in groups, with flat or tubular shapes of 4–40 μm in size; type IIb inclusions predominated in the Woxi deposit.

Type III inclusions are scarce in all the selected samples and are characterized by the vapour phase, which constitutes more than 60% of the total volume of the inclusion at room temperature. These inclusions form rounded rectangles and ellipsoids, which are 10–30 μm in diameter, and occur mainly in groups together with type I, type II, and/or type IV inclusions (Figs. 6B, 6E, 7B, 7D and 7G).

Type IV inclusions are rare and mainly found in scheelite and quartz-II samples. They display rounded rectangle shapes, with size varying from a few microns to 10 μm. These inclusions occur in isolation or in groups together with type II inclusions (Fig. 7D).

## 6. Results

### 6.1. Microthermometry

Microthermometric studies are mainly carried out on type I and type II inclusions in this study. The cycling method proposed by Goldstein and Reynolds (1994) was adopted for measuring the final melting temperature ($T_m$) and homogenization temperature ($T_h$) values in some inclusions whose phase transitions could not be clearly observed. Microthermometric results of fluid inclusions in scheelite and quartz-I from the quartz–scheelite veins as well as stibnite and quartz-II from the later quartz–sulfide–gold veins are summarized in Table 1.

#### 6.1.1. Scheelite

Type I inclusions have eutectic temperatures ($T_e$) ranging from −27.1 °C to −25.2 °C (Table 1). The final ice-melting temperature ($T_{m\text{-}ice}$) ranges from −3.6 °C to −2.8 °C (n = 14), corresponding to the salinities of 4.65–5.86 wt.% NaCl equiv. (Fig. 8A), with an average of 5.24 wt.% NaCl equiv. Homogenization temperatures ($T_h$) fall between 151.3 °C and 337.3 °C (n = 78), mostly in the range of 160–240 °C (Fig. 8B). The bulk densities of the ore-forming fluids vary from 0.86 to 0.94 g/cm$^3$.

Type IIb inclusions form solid $CO_2$ upon cooling below −95 °C. The final melting temperatures of the solid $CO_2$ phase ($T_{m\text{-}CO2}$) can reach from −62.7 °C to −56.7 °C (n = 8), indicative of some other volatile components mixed with $CO_2$, further identified as $N_2$ by laser Raman spectroscopy. For type IIb inclusions, the $CO_2$ phase homogenized to liquid ($T_{h\text{-}CO2}$) at the temperatures of 17.7–28.0 °C (n = 18, mean = 24.3 °C), and for type IIa, at 10.3 °C (Fig. 9A). The final clathrate-melting temperatures ($T_{m\text{-clathrate}}$) range from 8.6 °C to 9.1 °C (n = 16), corresponding to salinities of 1.81–2.77 wt.% NaCl equiv. (Fig. 8A). Although some type II inclusions decrepitate before total homogenization, others homogenized to the aqueous phase at the temperatures of 217.0–269.9 °C (n = 11, mostly between 240 °C and 270 °C) and to the $CO_2$ phase at 286.8 °C. In addition, two type IIa inclusions homogenized to the vapour phase at 258.7 °C and 263.4 °C (Fig. 8B). Their bulk densities range from 0.84 to 0.96 g/cm$^3$.

#### 6.1.2. Quartz-I

Eutectic temperature of type I inclusion in quartz-I ($T_e$ = −24.5 °C, Table 1) is similar to those measured in scheelite in this study. Type I inclusions have $T_{m\text{-}ice}$ with the range of −3.4 °C to −1.4 °C (n = 7), corresponding to salinities of 2.41–5.56 wt.% NaCl equiv. with a bimodal distribution (Fig. 8C). All type I fluid inclusions homogenized to the liquid phase at temperatures between 162.5 °C and 342.2 °C (n = 34, mostly 200–220 °C; Fig. 8D). The bulk densities of these fluid inclusions vary between 0.89 and 0.92 g/cm$^3$. Two inclusions of type IIb homogenized to the vapour phase at 258.6 °C and 357.0 °C, with $T_{h\text{-}CO2}$ (homogenized to the $CO_2$ liquid phase) of 24.3 °C and 26.3 °C, respectively (Fig. 9A). Type III inclusions are rare and only one has been measured in this study, it displays a homogenization temperature (to the vapour phase) of 353.6 °C (Fig. 8D).

#### 6.1.3. Stibnite

$T_{m\text{-}ice}$ of type I inclusions ranges from −3.1 °C to −1.3 °C (n = 39), corresponding to salinities varying from 2.24 to 5.11 wt.% NaCl equiv. (Fig. 10A), with an average of 3.2 wt.% NaCl equiv. Type I inclusions mainly homogenized to the liquid phase within the temperature range of 109.0–273.9 °C (n = 30), with one homogenized to the vapour phase at 190.0 °C, but most in the range of 140–180 °C (Fig. 10B). Two $T_h$ values (248.1 °C and 273.9 °C) of type I inclusions are significantly higher than their actual homogenization temperatures because leaking

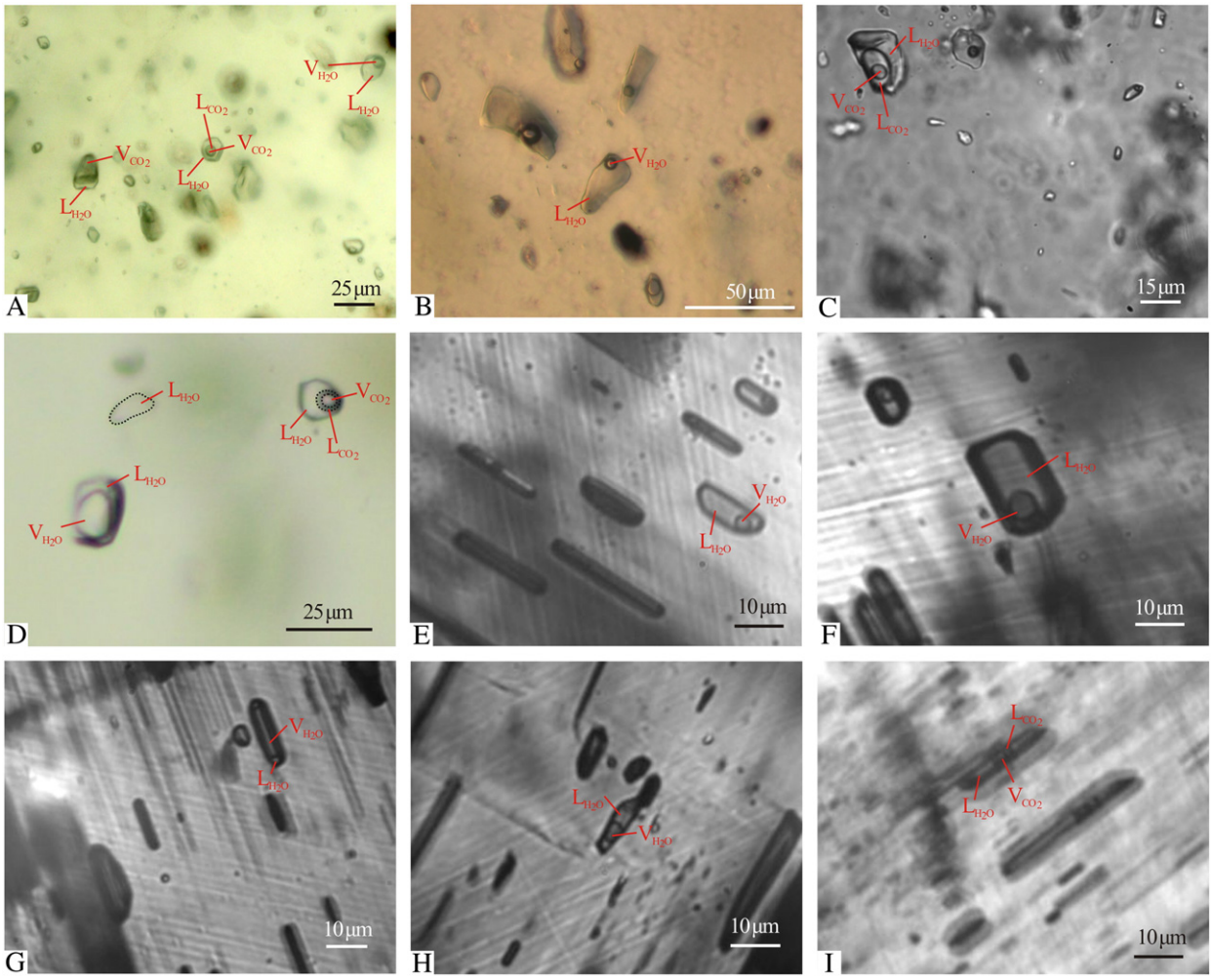


**Fig. 7.** Photomicrographs of representative fluid inclusion types at room temperature in quartz–sulfide–gold stage. (A) Coexistence of type I and type II inclusions in quartz-II. (B) Coexistence of type I with variable liquid/vapour ratios and type III inclusions in quartz-II. (C) Type II inclusions in quartz-II. (D) Coexistence of type II and type III and type IV inclusions in quartz-II. (E–F) Type I inclusions with tubular shape in stibnite. (G) Type III inclusion in stibnite. (H) Type I inclusion with irregular shape in stibnite. (I) Type II inclusions in stibnite.

probably takes place during heating. Their bulk densities fall in the range of 0.79–0.96 g/cm$^3$.

*6.1.4. Quartz-II*

Type I inclusions have $T_e$ with the range of −26.9 °C to −22.3 °C (Table 1). Their $T_{m\text{-}ice}$ values vary from −4.3 °C to −0.5 °C (n = 43), corresponding to the salinities of 0.88–6.88 wt.% NaCl equiv. (Fig. 10C), with an average of 3.47 wt.% NaCl equiv. These fluid inclusions homogenized to the liquid phase within the temperature range of 131.3 °C to 252.4 °C (n = 94), mostly varying between 160 °C and 200 °C (Fig. 10D). The bulk densities vary from 0.83 to 0.98 g/cm$^3$.

For type IIb inclusions, $T_{m\text{-}CO2}$ ranges from −57.8 °C to −55.8 °C (n = 16, mean = 56.6 °C). Their $T_{m\text{-}clathrate}$ values fall in between 9.4 °C and 10 °C (n = 17, mean = 9.7 °C), corresponding to the salinities of 0.02–1.22 wt.% NaCl equiv. (Fig. 10C). Some of the type IIb inclusions have $T_{m\text{-}clathrate}$ above 10 °C, always accompanied by $T_{m\text{-}CO2}$

**Table 1**
Microthermometric data in the Woxi deposit, western Hunan.

| Mineral | Type | Te (°C) | Tm-$CO_2$ (°C) | Th-$CO_2$ (°C) | Tm-clathrate or Tm-ice (°C) | Salinity | Th or Th-tot (→L) (°C) | Th or Th-tot (→V) (°C) | D (g/cm$^3$) |
|---|---|---|---|---|---|---|---|---|---|
| *Quartz–scheelite–wolframite stage* | | | | | | | | | |
| Quartz-I | I | −24.5 (1) | | | −3.4 to −1.4 (7) | 2.41–5.56 (7) | 162.5–342.2 (34) | | 0.89–0.92 (7) |
| | IIb | | | 24.3–26.3 (2) | | | | 258.6–357.0 (2) | |
| | III | | | | | | 353.6 (1) | | |
| Scheelite | I | −27.1 to −25.2 (2) | | | −3.6 to −2.8 (14) | 4.65–5.86 (14) | 151.3–337.3 (78) | | 0.85–0.94 (11) |
| | IIa | | | 10.3 (1) | | | | 258.7–263.4 (2) | |
| | IIb | | −62.7 to −56.7 (8) | 17.7–28.0 (18) | 8.6–9.1 (16) | 1.81–2.77 (16) | 217.0–269.9 (11) | 286.8 (1) | 0.84–0.96 (9) |
| *Quartz–sulfide–gold stage* | | | | | | | | | |
| Quartz-II | I | −22.3 to −26.9 (2) | | | −4.3 to −0.5 (43) | 0.88–6.88 (43) | 131.3–252.4 (94) | | 0.83–0.98 (42) |
| | IIb | | −57.8 to −55.8 (16) | 17.8–28.0 (26) | 9.4–10.0 (17) | 0.02–1.22 (17) | 189.5–246.2 (16) | | 0.91–0.96 (13) |
| Stibnite | I | | | | −3.1 to −1.3 (39) | 2.24–5.11 (39) | 109.0–273.9 (30) | 190.0 (1) | 0.79–0.96 (19) |

Note: Numbers in parentheses are the number of measurements. Salinity is in wt.% NaCl equiv.

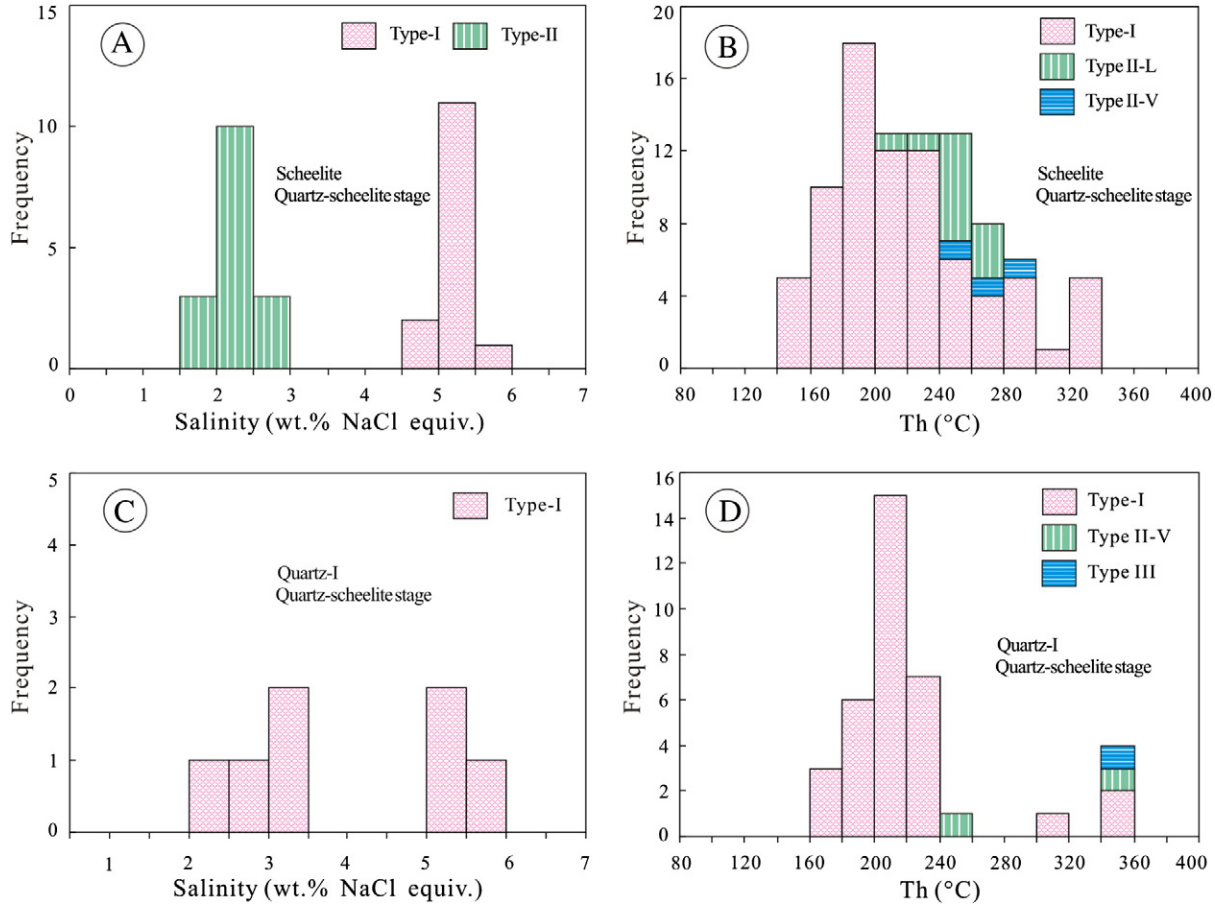


**Fig. 8.** Histograms of salinities and homogenization temperatures of fluid inclusions in scheelite (A–B) and coexisting quartz-I (C–D) collected from the Woxi deposit.

below −56.6 °C, indicating the presence of volatile components besides $CO_2$, which have been identified as $N_2$ by the laser Raman analyses. All the type IIb inclusions homogenized to the aqueous phase within the temperature range of 189.5 °C–357.8 °C (n = 16, mostly varying between 200 °C and 260 °C; Fig. 10D). $CO_2$ vapour phase homogenized to the liquid phase at temperatures between 17.8 °C and 28.0 °C (n = 26, mean = 23.0 °C) (Fig. 9B). Their corresponding bulk densities vary from 0.91 to 0.96 g/cm$^3$.

### 6.2. Raman spectroscopy

A detailed Raman spectroscopic analysis of fluid inclusions in quartz-I and quartz-II was performed. $CO_2$ is the major non-$H_2O$ volatile component in all fluid inclusions, and minor $N_2$ was also detected in some fluid inclusions (Fig. 11). The relative higher $N_2$ concentrations measured in the type II fluid inclusions are consistent with an obvious decrease of the melting point of pure $CO_2$ in these fluid inclusions.

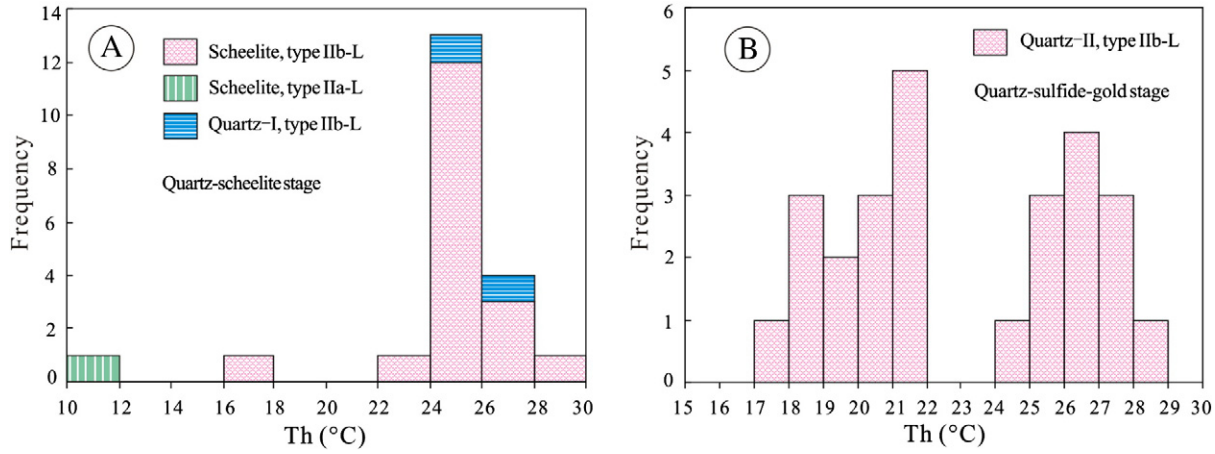


**Fig. 9.** Histograms of $CO_2$ homogenization temperatures in scheelite and quartz-I (A) and quartz-II (B) collected from the Woxi deposit.

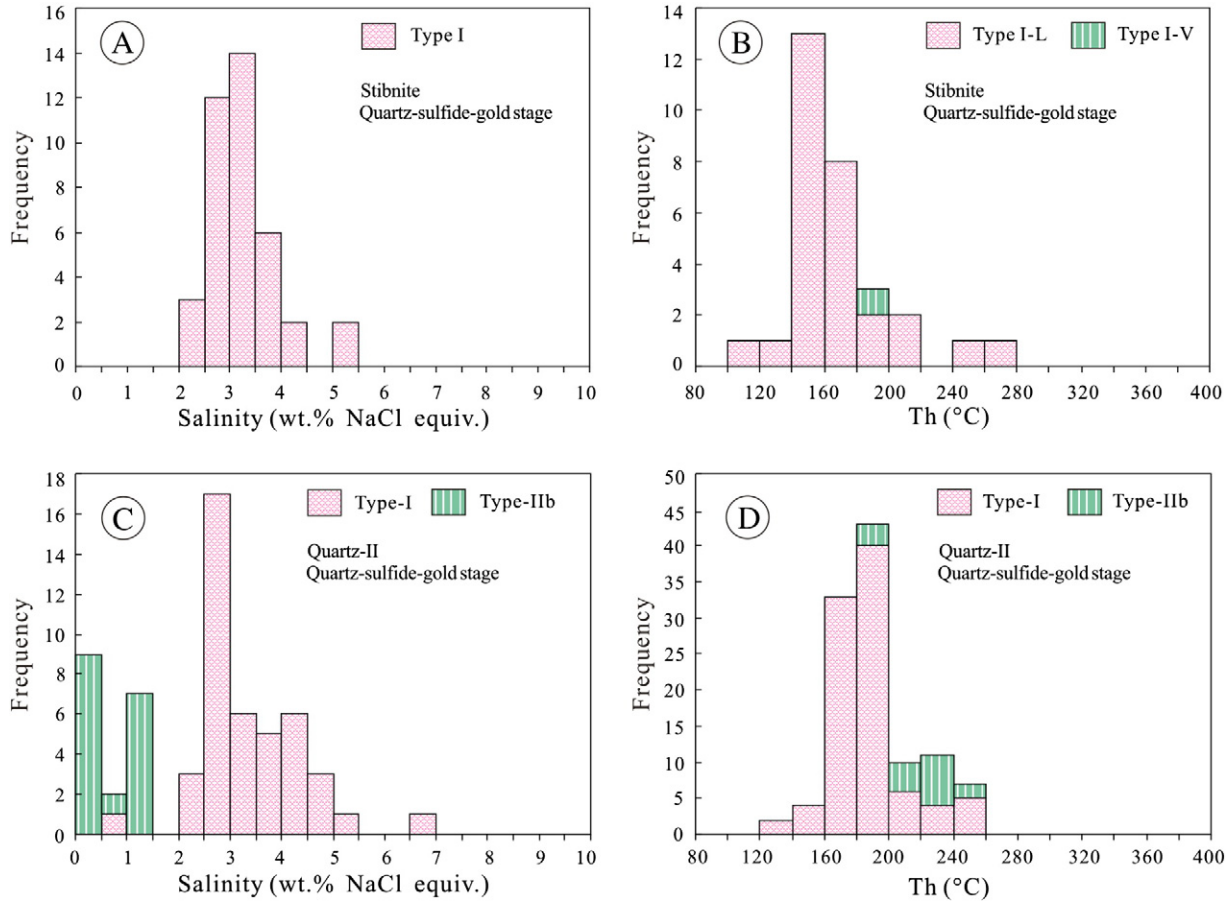


**Fig. 10.** Histograms of salinities and homogenization temperatures of fluid inclusions in stibnite (A–B) and coexisting quartz-II (C–D) collected from the Woxi deposit.

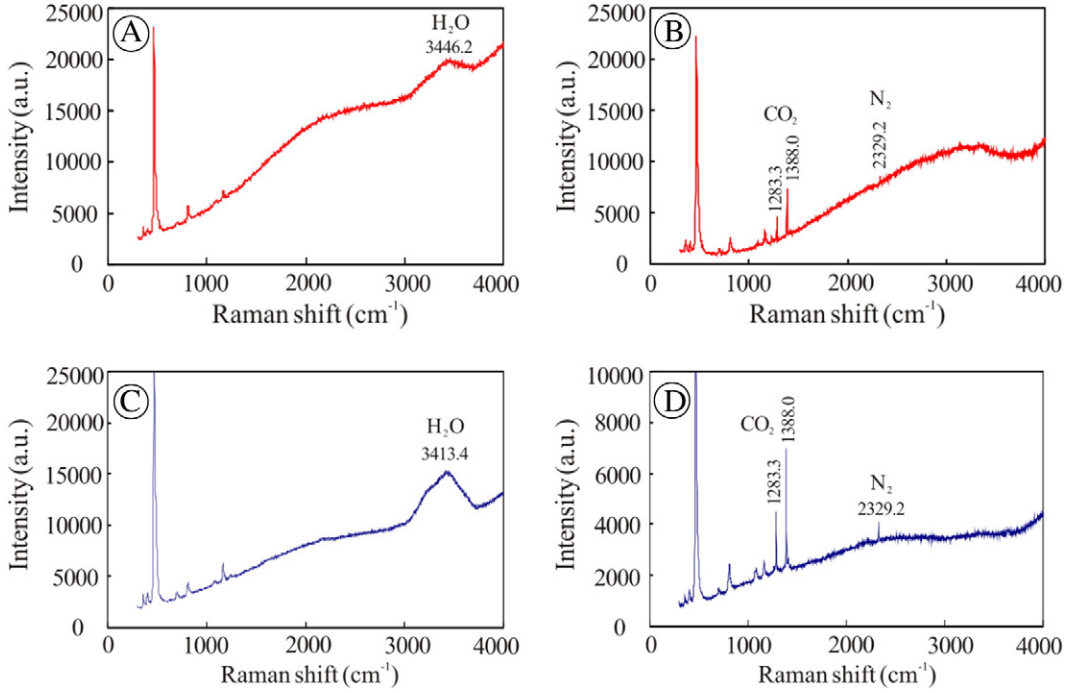


**Fig. 11.** Representative Raman spectra of fluid inclusions in quartz-I (A–B) of quartz–scheelite stage and quartz-II (C–D) of quartz–sulfide–gold stage. A and C show that the vapour bubbles are mainly of $H_2O$; B and D show that the bubbles contain some $N_2$ in addition to $CO_2$.

**Table 2**
Noble gas compositions and isotopic ratios of fluid inclusions trapped in pyrite and stibnite samples from the Woxi deposit, western Hunan.

| Sample | Mineral | $^3He$ ($E^{-12}$) | $^4He$ ($cm^3STP/g$) ($E^{-7}$) | $^{40}Ar$ ($cm^3STP/g$) ($E^{-7}$) | $^{36}Ar$ ($cm^3STP/g$) ($E^{-7}$) | $^3He/^4He$ (Ra) | $^{40}Ar/^{36}Ar$ | $^4He/^{36}Ar$ | $\%^{40}Ar_E$ | $F^4He$ |
|---|---|---|---|---|---|---|---|---|---|---|
| WX-119 | Pyrite | 0.021 | 428 | 10.22 | 0.008 | 0.005 | 1341.7 | 56,189 | 78 | 339,508 |
| WX-155 | Pyrite | 0.009 | 417 | 4.41 | 0.007 | 0.002 | 624.2 | 59,023 | 53 | 356,634 |
| XXJK-34 | Pyrite | 0.017 | 396 | 1.97 | 0.001 | 0.004 | 2585.9 | 519,805 | 89 | 3,140,817 |
| WX-159 | Pyrite | 0.025 | 486 | 2.05 | 0.003 | 0.005 | 722.2 | 171,214 | 59 | 1,034,527 |
| XXJK-33 | Pyrite | 0.047 | 551 | 11.34 | 0.008 | 0.009 | 1446.1 | 70,265 | 80 | 424,560 |
| XXJK-35 | Pyrite | 0.097 | 512 | 2.63 | 0.004 | 0.019 | 698.1 | 135,904 | 58 | 821,171 |
| WX-121 | Pyrite | 0.030 | 166 | 5.00 | 0.003 | 0.018 | 1715.9 | 56,968 | 83 | 344,217 |
| WX-146 | Pyrite | 0.038 | 522 | 5.92 | 0.011 | 0.007 | 528.8 | 46,659 | 44 | 281,926 |
| WX-27-3 | Pyrite | 0.486 | 294 | 2.49 | 0.009 | 0.165 | 281.3 | 33,240 | – | 200,849 |
| WX-24-5 | Pyrite | 0.112 | 80 | 1.15 | 0.005 | 0.139 | 247.0 | 17,176 | – | 103,785 |
| WX-27-1 | Pyrite | 0.304 | 356 | 2.93 | 0.008 | 0.086 | 388.6 | 47,269 | 24 | 285,615 |
| WX-23-12 | Pyrite | 0.111 | 139 | 1.80 | 0.007 | 0.080 | 264.2 | 20,445 | – | 123,537 |
| XXJK-21 | Pyrite | 0.036 | 156 | 5.15 | 0.022 | 0.023 | 229.9 | 6990 | – | 42,235 |
| WX-23-10 | Stibnite | 0.005 | 7 | 9.39 | 0.027 | 0.063 | 347.8 | 275 | 15 | 1663 |
| WX-28-5 | Stibnite | 0.366 | 130 | 15.24 | 0.036 | 0.281 | 420.0 | 3591 | 30 | 21,698 |
| WX-34-4 | Stibnite | 0.004 | 17 | 13.29 | 0.051 | 0.022 | 260.3 | 328 | – | 1983 |
| YRS-15 | Stibnite | 0.005 | 11 | 7.53 | 0.024 | 0.044 | 313.6 | 470 | 6 | 2843 |
| WX-24-8 | Stibnite | 0.016 | 62 | 20.82 | 0.042 | 0.026 | 495.0 | 1471 | 40 | 8887 |
| XXJK-15 | Stibnite | 0.014 | 50 | 7.01 | 0.015 | 0.028 | 468.4 | 3310 | 37 | 20,000 |

Note: $F^4He$ values reflect enrichment of $^4He$ in the fluid relative to air; $F^4He = (^4He / ^{36}Ar)_{sample} / (^4He / ^{36}Ar)_{air}$ where $(^4He / ^{36}Ar)_{air} = 0.1655$ (Kendrick et al., 2001).

### 6.3. Noble gas isotopes

Pyrite and stibnite samples analysed in this study are well-crystallized euhedral grains without any obvious subsequent deformation. With the exception of eight pyrite samples collected from the altered wall rocks, all the remaining samples show a paragenesis with quartz-II in the quartz–sulfide–gold veins. Therefore, we are confident that the extracted fluids from those sulfides (especially from the veins) are related to hydrothermal mineralization, and thus they should be identical to the fluid inclusions hosted in the quartz-II and stibnite in this study. Because in-situ additions of radiogenic $^4He$ and $^{40}Ar$ and cosmogenic nuclides are negligible for these sulfide samples collected from underground exposures, the measured compositions of noble gas isotopes can truly represent the initial composition of the fluid inclusions.

The noble gas isotope compositions of fluid inclusions in the samples mentioned above are listed in Table 2. The data show that $^4He$ concentrations vary from 7 to $551 \times 10^{-7}$ $cm^3STP/g$ and $^{40}Ar$ concentrations fall in between 1.15 and $20.82 \times 10^{-7}$ $cm^3STP/g$. The $^3He/^4He$ ratios vary in the range of 0.002–0.281 Ra ($Ra = 1.4 \times 10^{-6}$ for air). The $^{40}Ar/^{36}Ar$ ratios vary from 229.9 to 2585.9. The $F^4He$ values for the hydrothermal fluids at Woxi, defined as $F^4He = (^4He / ^{36}Ar)_{sample} / (^4He / ^{36}Ar)_{air}$ where $(^4He / ^{36}Ar)_{air} = 0.1655$ (Kendrick et al., 2001), are above 1000 (Table 2).

## 7. Discussion

### 7.1. Nature of ore-forming fluids

At the quartz–scheelite stage, fluid inclusions trapped in scheelite and quartz-I display the same types (Fig. 6) and largely share similar temperatures and salinities (Fig. 8). The majority of fluid inclusions in scheelite and quartz-I have homogenization temperatures in the range of 180–240 °C and 200–220 °C, respectively. The salinities of fluid inclusions in quartz-I and scheelite exhibit a bimodal distribution (Fig. 8A and C). Some fall in between 1.5 and 3.5 wt.% NaCl equiv. with a mode around 2.0 wt.% NaCl equiv., while the others vary between 4.5 and 6.0 wt.% NaCl equiv. with a mode at 5.0 wt.% NaCl equiv. The lower salinities in scheelite were determined from the final clathrate-melting temperatures of type II inclusions, and those relatively higher salinities were determined from the final ice-melting temperatures of type I inclusions. However, all the lower and higher salinity inclusions in quartz-I were determined from the final ice-melting temperatures of type I inclusions. An alternative explanation for the low salinities for type I inclusions in quartz-I is that these inclusions also contain minor heterogeneously-trapped $CO_2$ (but undetected by the conventional petrography observations and microthermometric measurement) (Guillemette and Williams-Jones, 1993). Such heterogeneous entrapment of $CO_2$ will result in anomalously high homogenization temperatures (Guillemette and Williams-Jones, 1993), which is consistent with the higher homogenization temperatures of the quartz-I hosted type I inclusions determined in this study (Fig. 8D). Therefore, it can be concluded that the fluid inclusions in scheelite and quartz-I probably have been trapped under a similar condition during the tungsten mineralization, consistent with the intergrown texture of scheelite and quartz-I in these samples.

At the quartz–sulfide–gold stage, most inclusions in stibnite are type I, whereas quartz-II hosts a range of inclusion types (except type IV) (Fig. 7A–I). Fluid inclusions in stibnite and quartz-II display similar microthermometric results (Fig. 10). Homogenization temperatures of fluid inclusions in stibnite mostly vary from 140 to 180 °C (Fig. 10B), and those in quartz-II fall in between 160 and 200 °C (Fig. 10D). Salinities of fluid inclusions in stibnite and quartz-II are mostly in the range of 2.5–4.0 wt.% NaCl equiv. and 2.5–4.5 wt.% NaCl equiv., respectively (Fig. 10A, C). This is consistent with the fact that stibnite commonly coexists with quartz-II (Fig. 4F).

According to many previous studies (e.g. Bailly et al., 2000; Campbell and Panter, 1990; Wang et al., 2013; Wei et al., 2012), the homogenization temperatures and salinities of fluid inclusions in ore minerals are distinct from those in coexisting gangue minerals. However, the consistency of fluid inclusions in ore minerals and gangue minerals also have been previously reported (e.g. Kucha and Raith, 2009). In this study, fluid inclusions in ore minerals (scheelite and stibnite) and their corresponding coexisting quartz share similar characteristics. The ore-forming fluids of the Woxi deposit are characterized by low-to-moderate temperatures, low salinities, $CO_2$-rich and $N_2$-bearing aqueous fluids. Likewise, fluid inclusions from other lode gold deposits in the Xuefengshan Range mainly include $H_2O$-rich aqueous inclusions and $CO_2$-rich inclusions with large variable liquid/vapour ratios. Their homogenization temperatures range from 100 °C to 330 °C (mostly 150–200 °C) and their salinity values are lower than 9 wt.% NaCl equiv. (Chen and Yu, 1994; Ding and Wang, 2009; He et al., 1996; Lu et al., 2012; Niu and Ma, 1991; Yao and Zhu, 1993; Yu, 1997). Minor components of $N_2$ and/or $CH_4$ are also detected in the vapour phase by laser Raman spectroscopy (Lu et al., 2012).

### 7.2. Sources of ore-forming fluids

The ore-forming fluids characterized by $CO_2$-rich may be derived from magmatic water (Fan et al., 2003; Yang et al., 2012, 2013), metamorphic water (Fairmaid et al., 2011; Goldfarb et al., 1988; Harlov, 2012; Lamadrid et al., 2013; Lawrence et al., 2013) or mantle (Luque et al., 2014; Mao et al., 2003; Tripathi et al., 2012; Xu et al., 2013). Although previous studies reveal that the $\delta^{18}O$ values of mineralization fluids in the Woxi deposit vary between 2.0‰ and 13.6‰ (Chen, 2012; Luo et al., 1984), these oxygen data cannot discriminate between a metamorphic or magmatic or evolved meteoric source.

The noble gas data determined in this study allow us to further evaluate these possible sources for the ore-forming hydrothermal fluids. Compared with the higher concentrations of $^4He$ in coexisting pyrite from veins ($80–356 \times 10^{-7}$ $cm^3$ STP/g), the lower values in intergrown stibnite ($7–130 \times 10^{-7}$ $cm^3$ STP/g) can be best explained by He loss (e.g. Hu et al., 1999b), since the helium diffusion is extremely slow in pyrite (Baptiste and Fouquet, 1996). However, the $^3He/^4He$ ratios for stibnite (mean of 0.099 Ra) are similar to those for coexisting pyrite (mean of 0.077 Ra), indicating that the mass fractionation of He caused by He loss in stibnite could be negligible (Fig. 12). The extremely low concentrations of $^3He$ ($0.009–0.486 \times 10^{-12}$ $cm^3$ STP/g) in pyrite and helium isotope ratios (0.002–0.281 Ra) in all pyrite and stibnite provide reliable evidence that He can't be originated from a mantle source ($>3 \times 10^{-12}$ $cm^3$ STP/g, Burnard et al., 1999; or 7–9 Ra, Ozima and Podosek, 2002).

Because even small magmatic additions to crustal fluid systems are readily detected (Ballentine et al., 2002), the involvement of magmatic fluids in many hydrothermal deposits are characterized by $^3He/^4He$ ratios commonly more than 0.1 Ra (e.g. Burnard et al., 1999; Sun et al., 2009; Zhu et al., 2013). In South China, the maximum $^3He/^4He$ ratios for many intrusion-associated gold, tungsten, and tin deposits are above 1 Ra (Burnard et al., 1999; Cai et al., 2012; Hu et al., 1997, 1999a, 2004; Sun et al., 2006; Zhai et al., 2012). Nevertheless, in the Woxi deposit, with the exception of sample WX-27-3 (0.165 Ra), WX-24-5 (0.139 Ra) and WX-28-5 (0.281 Ra), all the helium isotope ratios in the remaining samples are less than 0.1 Ra (Table 2). This probably indicates that the ore-forming fluids responsible for gold, antimony, and tungsten mineralization in Woxi are not of magmatic in origin. Moreover, as the $F^4He$ values for sulfides in this study (>1000, Table 2) are remarkably higher than that for the atmosphere ($F^4He = 1$, Kendrick et al., 2001) and ASW ($F^4He = 0.18–0.28$, Kendrick et al., 2001), the fluids in Woxi probably contain negligible contributions from atmospheric He, the measured $^3He/^4He$ ratios are probably derived from a crustal He source.

The estimated $^{40}Ar/^{36}Ar$ ratios range from 229.9 to 2585.9 (Table 2). $^{40}Ar/^{36}Ar$ values lower than the atmospheric ratio of 295.5 have mainly been interpreted to be the result of mass fractionation (Nagao et al., 1979, 1981; Schaaf and MÜller-Sohnius, 2002; Singer and Brown, 2002) and perhaps require a non-geological explanation (Singer and Brown, 2002), while those higher than 295.5 indicate a significant proportion of excess $^{40}Ar$ ($^{40}Ar_E$) from a mantle or crustal origin. Because a minor addition of mantle component will dramatically change the He isotopic composition, the $^{40}Ar_E$ (up to 89%, Table 2) is probably derived from a crustal source rather than a mantle component, and might be generated by the host rocks or old basement (Fairmaid et al., 2011; Kendrick et al., 2002). This is consistent with the extremely high Sr isotope compositions in scheelite (0.743–0.750; Peng et al., 2003b; Peng and Frei, 2004) and in fluid inclusions in quartz coexisting with stibnite (0.754–0.766; Shi et al., 1993) in this deposit, which has been considered to be a result of either preferential leaching of Proterozoic rocks or leaching of the underlying older rocks (Peng et al., 2003b).

### 7.3. Mineralization mechanism

Mixing and boiling are the most important physical processes affecting ore deposition (Wilkinson, 2001). Fluid mixing has been recognized in many tungsten deposits worldwide (e.g. Beuchat et al., 2004; Wei et al., 2012; Yokart et al., 2003). Noticeably, boiling is an efficient mechanism for gold precipitation in many lode gold deposits (e.g. Sigma deposit, Canada, Robert and Kelly, 1987; Bronzewing deposit, Australia, Dugdale and Hagemann, 2001; Wiluna deposits, Australia, Hagemann and Lüders, 2003; Wangfeng deposit, China, Zhang et al., 2012), and some stibnite deposits (Bailly et al., 2000; Guillemette and Williams-Jones, 1993).

In the Woxi deposit, during the early quartz–scheelite stage, the fluids contain variable amounts of $N_2$ suggesting that the mineralizing solutions reacted either directly with the host rocks or with fluids trapped within the host rocks (Mernagh, 2001; Polito et al., 2001). Peng et al. (2005) also proposed that aqueous effects or water–rock interaction is responsible for scheelite precipitation in Woxi based on the REE tetrad-effect characteristics in scheelite. Moreover, a positive relationship between homogenization temperatures and salinities of most aqueous inclusions in scheelite and quartz-I as shown in Fig. 13, further reveals that a hotter, saline fluid mixed with a cooler, dilute fluid (Wilkinson, 2001). Therefore, fluid mixing between deep crustal fluid and host-rock-buffered fluid is a possible mechanism associated with scheelite precipitation in the Woxi deposit.

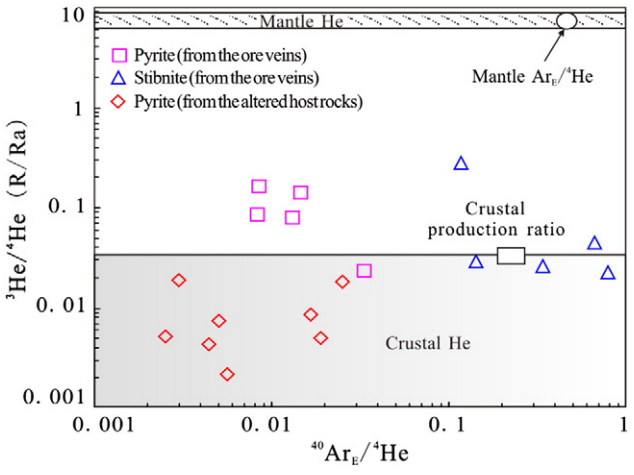


**Fig. 12.** $^3He/^4He$ vs. $^{40}Ar_E/^4He$ diagram for fluid inclusions in pyrite and stibnite collected from the Woxi deposit.

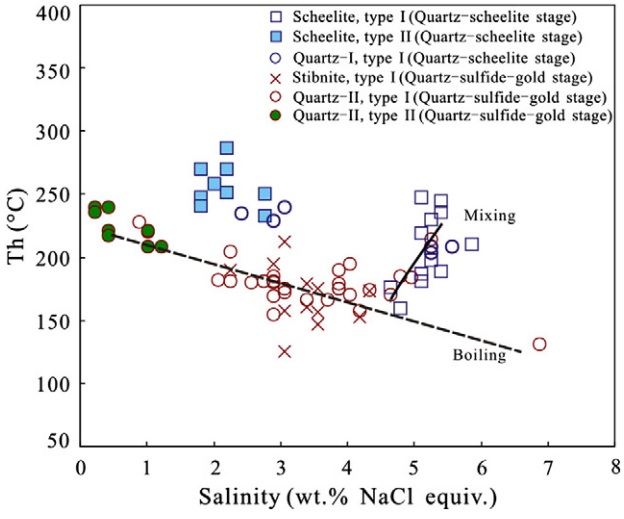


**Fig. 13.** Homogenization temperature vs. salinity of different types of fluid inclusions at the quartz–scheelite stage and quartz–sulfide–gold stage.

In contrast, fluid inclusion petrography and microthermometric data for the quartz–sulfide–gold stage provide evidence for boiling. Three types of fluid-inclusion assemblages are observed: (1) type I, IIa, and IIb inclusions (Fig. 7A); (2) type I aqueous inclusions with considerable variable liquid/vapour ratios and type III inclusions (Fig. 7B); (3) type IIb, III, and IV inclusions (Fig. 7D). All fluid-inclusion assemblages usually display roughly similar homogenization temperature, indicative of fluid boiling (Ramboz et al., 1982; Van den Kerkhof and Hein, 2001; Wilkinson, 2001). A negative correlation between the homogenization temperature and salinity for most inclusions (Fig. 13), and the common occurrence of $H_2O$-rich, higher salinity inclusions coexisting with $CO_2$-rich, lower salinity type II inclusions in this study can also be best explained by fluid boiling (Chen et al., 2012b; Fan et al., 2009; Liu et al., 2013; Mernagh, 2001; Pichavant et al., 1982; Wilkinson, 2001). Previous studies suggest that $H_2S$ prefers to enter the vapour phase during boiling, and sulfur decrease in the fluids probably results in gold deposition (Guillemette and Williams-Jones, 1993; Naden and Shepherd, 1989). Thus, it can be concluded that boiling is critical for gold and stibnite deposition in the Woxi deposit.

Moreover, boiling is probably caused by an abrupt drop in pressure (Wilkinson, 2001) induced by the fault-valve mechanism (McCuaig and Kerrich, 1998; Sibson et al., 1988) in hydrothermal systems, because structural evidences for fluid-pressure fluctuations shown in Figs. 3D–F and 4A–E are common in the Woxi mining district. In order to evaluate the fluid-pressure conditions at the time of entrapment, the isochores of type I inclusions were estimated by the online calculation (gcmodel.kl-edi.ac.cn/archives/); the isochores of type II inclusions were calculated with the equation of state for $NaCl–H_2O–CO_2$ proposed by Brown and Lamb (1989). At 182 °C, which is the average homogenization temperature of type I fluid inclusions at the quartz-sulfide-gold stage, the pressure is estimated to be between 960 and 1850 bars.

### 7.4. Orogenic-type model for the Woxi Au–Sb–W deposit

Several genetic models have been proposed for this deposit, including (1) a sedimentary exhalative (SEDEX) origin (Gu et al., 2007, 2012; Zhang, 1985), (2) a magmatic-hydrothermal origin (Mao and Li, 1997; Peng and Frei, 2004), and (3) a metamorphic-hydrothermal origin (Luo et al., 1984; Yang, 1992). However, the low salinity, $CO_2$-rich and $N_2$-bearing aqueous fluid associated with Au–Sb–W mineralization at Woxi is significantly different from the SEDEX type deposits, the latter usually have higher salinity (3.5–15 wt.% NaCl equiv.) without $CO_2$-rich fluid inclusions (Canet et al., 2003; Chen et al., 2007; Lott et al., 1999). The marked radiogenic $^{87}Sr$-rich ore-forming fluids (0.743–0.750; Peng et al., 2003b; Peng and Frei, 2004) for the Woxi deposit is not compatible with a SEDEX origin (Peng et al., 2003b). Whereas, the relatively low temperature and salinity values for the Woxi deposit are different to those typical for magmatic-hydrothermal deposits.

Instead, the geological and geochemical features documented in Woxi are compatible with orogenic gold deposits (Goldfarb et al., 2005; Groves et al., 1998; Groves et al., 2003; Kerrich et al., 2000; McCuaig and Kerrich, 1998; Ridley and Diamond, 2000). The Woxi deposit occurs in an intracontinental orogenic setting of the Xuefengshan Range (Chu et al., 2012; Li et al., 2009; Zhang et al., 2013). Orebodies are predominantly quartz veins with minor pyrite, which are hosted by shear zones in metamorphosed turbidites. Moreover, the low-to-moderate temperature, low-salinity, $H_2O–CO_2–NaCl$ deeply-derived crustal fluid with $\delta^{18}O$ and $\delta D$ values (2.0–13.6‰, −81 to −64‰; Luo et al., 1984; Chen, 2012) at Woxi is consistent with many orogenic gold fluid studies worldwide (e.g. Goldfarb et al., 2001; Groves et al., 1998; Kerrich et al., 2000). However, compared to gold-only orogenic deposits, the Woxi deposit exhibits the atypical element association of Au–Sb–W, thus setting it apart from most orogenic gold deposits.

## 8. Conclusions

(1) In the Woxi Au–Sb–W deposit, the fluid inclusions in ore minerals and corresponding intergrown quartz largely share similar characteristics, and yield homogenization temperatures of 180–240 °C in the quartz–scheelite veins, and 140–200 °C in later quartz–sulfide–gold veins.
(2) The ore-forming fluids in Woxi are characterized by low salinity, low-to-moderate temperature, $CO_2$-rich and $N_2$-bearing aqueous fluids, consistent with other lode gold deposits in the Xuefengshan Range. They are dominated by deeply non-magmatic crustal origin fluids, with a minor contribution of meteoric water or wallrock-buffered fluid.
(3) Fluid mixing is a possible mechanism for early scheelite precipitation, but boiling caused by the marked pressure drop is critical to gold and stibnite deposition in the Woxi deposit.
(4) The Woxi Au–Sb–W deposit is probably an atypical orogenic gold deposit with significant tungsten and antimony mineralization.

## Acknowledgments

This work was financially supported by the National Natural Science Foundation of China (Grants No. 40673021, 41073036, 41272096) and the National Special Research Programs for Non-Profit Trades (Sponsored by MLR, Grant No. 200911007). The authors give special thanks to the geologists and miners of the Woxi mining district, for their enthusiastic help during the field investigation. Prof. Su Wen-Chao is thanked for his warm-hearted help during data processing. Prof. Lu Huan-Zhang is acknowledged for his comments on the microthermometric results. Our thanks are also due to an anonymous reviewer for the careful and constructive comments and suggestions, which significantly improved the manuscript. Lastly, critical reviews by Prof. Franco Pirajno are greatly appreciated.

## References

Bailly, L., Bouchot, V., Beny, C., Milesi, J.P., 2000. Fluid inclusion study of stibnite using infrared microscopy: an example from the Brouzils antimony deposit (Vendee, Armorican massif, France). Econ. Geol. Bull. Soc. 95, 221–226.
Bailly, L., Grancea, L., Kouzmanov, K., 2002. Infrared microthermometry and chemistry of wolframite from the Baia Sprie epithermal deposit, Romania. Econ. Geol. 97, 415–423.
Ballentine, C.J., Burgess, R., Marty, B., 2002. Tracing fluid origin, transport and interaction in the crust. In: Porcelli, D., Ballentine, C.J., Wieler, R. (Eds.), Noble Gases in Geochemistry and Cosmochemistry, pp. 539–614.
Baptiste, P.J., Fouquet, Y., 1996. Abundance and isotopic composition of helium in hydrothermal sulfides from the East Pacific Rise at 13°N. Geochim. Cosmochim. Acta 60, 87–93.
Beuchat, S., Moritz, R., Pettke, T., 2004. Fluid evolution in the W–Cu–Zn–Pb San Cristobal vein, Peru: fluid inclusion and stable isotope evidence. Chem. Geol. 210, 201–224.
Bodnar, R.J., 1993. Revised equation and table for determining the freezing-point depression of $H_2O$–NaCl solutions. Geochim. Cosmochim. Acta 57, 683–684.
Brown, P.E., Lamb, W.M., 1989. P–V–T properties of fluids in the system $H_2O \pm CO_2 \pm$ NaCl: new graphical presentations and implications for fluid inclusion studies. Geochim. Cosmochim. Acta 53, 1209–1221.
Bruno, L.A., Baur, H., Graf, T., Schlüchter, C., Signer, P., Wieler, R., 1997. Dating of Sirius Group tillites in the Antarctic Dry Valleys with cosmogenic $^{3}He$ and $^{21}Ne$. Earth Planet. Sci. Lett. 147, 37–54.
Buchholz, P., Oberthür, T., Lüders, V., Wilkinson, J., 2007. Multistage Au–As–Sb Mineralization and crustal-scale fluid evolution in the Kwekwe District, Midlands Greenstone Belt, Zimbabwe: a combined geochemical, mineralogical, stable isotope, and fluid inclusion study. Econ. Geol. 102, 347–378.
Burgess, R., Taylor, R.P., Fallick, A.E., Kelley, S.P., 1992. $^{40}Ar/^{39}Ar$ laser microprobe study of fluids in different colour zones of a hydrothermal scheelite crystal from the Dae Hwa W–Mo mine, South Korea. Chem. Geol. 102, 259–267.
Burnard, P.G., Hu, R.Z., Turner, G., Bi, X.W., 1999. Mantle, crustal and atmospheric noble gases in Ailaoshan gold deposits, Yunnan Province, China. Geochim. Cosmochim. Acta 63, 1595–1604.
Cai, M.H., Wang, X.B., Keisuke, N., Peng, Z.N., Guo, T.F., Liu, H., Tan, Z.M., 2012. Noble gas isotopic characteristics of Hehuaping tin-polymetallic deposit, southern Hunan Province. Mineral Deposits 31, 1163–1170 (in Chinese with English abstract).
Campbell, A.R., Panter, K.S., 1990. Comparison of fluid inclusions in coexisting (cogenetic?) wolframite, cassiterite, and quartz from St. Michael's Mount and Cligga Head, Cornwall, England. Geochim. Cosmochim. Acta 54, 673–681.
Campbell, A.R., Robinson-Cook, S., 1987. Infrared fluid inclusion microthermometry on coexisting wolframite and quartz. Econ. Geol. 82, 1640–1645.

Campbell, A.R., Hackbarth, C.J., Plumlee, G.S., Petersen, U., 1984. Internal features of ore minerals seen with the infrared microscope. Econ. Geol. 79, 1387–1392.
Canet, C., Alfonso, P., Melgarejo, J.C., Fallick, A.E., 2003. Origin of the mineralizing fluids from the Carboniferous sedex deposits of L'Alforja (SW Catalonian Coastal Ranges, Spain). J. Geochem. Explor. 78–79, 513–517.
Chen, Y.J., 2006. Orogenic-type deposits and their metallogenic model and exploration potential. Geol. China 33, 1181–1196 (in Chinese with English abstract).
Chen, A.Q., 2012. Study on Mineralization Regularity and Formation Mechanism of Scheelite and Wolframite in the Woxi Au–Sb–W Deposit in Hunan Province (M.Sc. Thesis) Chinese University of Geosciences (Beijing), Beijing, pp. 1–66 (in Chinese with English abstract).
Chen, Y.D., Yu, D.L., 1994. Study of fluid inclusions of vein-type gold deposits and its implication to predict for blind orebodies in wester Hunan and eastern Guizhou. Guizhou Geol. 11, 280–286 (in Chinese with English abstract).
Chen, Y.J., Ni, P., Fan, H.R., Pirajno, F., Lai, Y., Su, W.C., Zhang, H., 2007. Diagnostic fluid inclusions of different types hydrothermal gold deposits. Acta Petrol. Sin. 23, 2085–2108 (in Chinese with Enlish abstract).
Chen, H.Y., Chen, Y.J., Baker, M.J., 2012a. Isotopic geochemistry of the Sawayaerdun orogenic-type gold deposit, Tianshan, northwest China: implications for ore genesis and mineral exploration. Chem. Geol. 310–311, 1–11.
Chen, H.Y., Chen, Y.J., Baker, M.J., 2012b. Evolution of ore-forming fluids in the Sawayaerdun gold deposit in the southwestern Chinese Tianshan metallogenic belt, Northwest China. J. Asian Earth Sci. 49, 131–144.
Chu, Y., Lin, W., Faure, M., Wang, Q.C., Ji, W.B., 2012. Phanerozoic tectonothermal events of the Xuefengshan Belt, central South China: implications from U–Pb age and Lu–Hf determinations of granites. Lithos 150, 243–255.
De Boorder, H., 2012. Spatial and temporal distribution of the orogenic gold deposits in the Late Palaeozoic Variscides and Southern Tianshan: how orogenic are they? Ore Geol. Rev. 46, 1–31.
Ding, Q.F., Wang, G., 2009. Study on fluid inclusions and genesis of Mobin gold deposit in Hunan Province. Glob. Geol. 28, 467–475 (in Chinese with English abstract).
Ding, B.Y., Yang, Y.Z., Liao, F.X., 1981. The fluid inclusion study and metallogeny review on gold deposits in western Hunan district. Central-South Inst Mining Metall 12, 114–120 (in Chinese with English abstract).
Dong, S.Y., Gu, X.X., Schulz, O., Vavtar, F., Liu, J.M., Zheng, M.H., Cheng, W.B., 2008. Fluid inclusion evidence for the genesis of the Woxi W–Sb–Au deposit, Hunan province. Acta Geol. Sin. 82, 641–647 (in Chinese with English abstract).
Dugdale, A.L., Hagemann, S.G., 2001. The Bronzewing lode-gold deposit, Western Australia: P–T–X evidence for fluid immiscibility caused by cyclic decompression in gold-bearing quartz-veins. Chem. Geol. 173, 59–90.
Fairmaid, A.M., Kendrick, M.A., Phillips, D., Fu, B., 2011. The origin and evolution of mineralizing fluids in a sediment-hosted orogenic-gold deposit, Ballarat East, Southeastern Australia. Econ. Geol. 106, 653–666.
Fan, H.R., Zhai, M.G., Xie, Y.H., Yang, J.H., 2003. Ore-forming fluids associated with granite-hosted gold mineralization at the Sanshandao deposit, Jiaodong gold province, China. Mineral. Deposita 38 (6), 739–750.
Fan, H.R., Hu, F.F., Wilde, S.A., Yang, K.F., Jin, C.W., 2009. The Qiyugou gold-bearing breccia pipes, Xiong'ershan region, central China: fluid-inclusion and stable-isotope evidence for an origin from magmatic fluids. Int. Geol. Rev. 53 (1), 25–45.
Fu, B., Kendrick, M., Fairmaid, A., Phillips, D., Wilson, C.L., Mernagh, T., 2012. New constraints on fluid sources in orogenic gold deposits, Victoria, Australia. Contrib. Mineral. Petrol. 163, 427–447.
Giamello, M., Protano, G., Riccobono, F., Sabatini, G., 1992. The W–Mo deposit of Perda Majori (SE Sardinia, Italy): a fluid inclusion study of ore and gangue minerals. Eur. J. Mineral. 4, 1079–1084.
Gold Headquarters of Chinese People's Armed Police Force (GHCPAPF), 1996. Geology of Woxi-type Stratabound Gold Deposit in Hunan Province. Seismological Press, Beijing, pp. 1–313 (in Chinese with English abstract).
Goldfarb, R.J., Leach, D.L., Pickthorn, W.J., Paterson, C.J., 1988. Origin of lode-gold deposits of the Juneau gold belt, southeastern Alaska. Geology 16 (5), 440–443.
Goldfarb, R.J., Groves, D.I., Gardoll, S., 2001. Orogenic gold and geologic time: a global synthesis. Ore Geol. Rev. 18 (1–2), 1–75.
Goldfarb, R.J., Baker, T., Dube, B., Groves, D.I., Hart, C.J., Gosselin, P., 2005. Distribution, character, and genesis of gold deposits in metamorphic terranes. Economic Geology 100th Anniversary Volume, pp. 407–450.
Goldstein, R.H., Reynolds, T.J., 1994. Systematics of Fluid Inclusions in Diagenetic Minerals. Society for Sedimentary Geology, Tulsa, pp. 1–199.
Groves, D.I., Goldfarb, R.J., Gebre-Mariam, M., Hagemann, S.G., Robert, F., 1998. Orogenic gold deposits: a proposed classification in the context of their crustal distribution and relationship to other gold deposit types. Ore Geol. Rev. 13, 7–27.
Groves, D.I., Goldfarb, R.J., Robert, F., Hart, C.J.R., 2003. Gold deposits in metamorphic belts: overview of current understanding, outstanding problems, future research, and exploration significance. Econ. Geol. 98, 1–29.
Groves, D.I., Condie, K.C., Goldfarb, R.J., Hronsky, J.M.A., Vielreicher, R.M., 2005. Secular changes in global tectonic processes and their influence on the temporal distribution of gold-bearing mineral deposits. Econ. Geol. 100, 203–224.
Gu, X.X., Oskar, S., Franz, V., Liu, J.M., Zheng, M.H., Fu, S.H., 2007. Rare earth element geochemistry of the Woxi W–Sb–Au deposit, Hunan province, South China. Ore Geol. Rev. 31, 319–336.
Gu, X.X., Zhang, Y.M., Schulz, O., Vavtar, F., Liu, J.M., Zheng, M.H., Zheng, L., 2012. The Woxi W–Sb–Au deposit in Hunan, South China: an example of Late Proterozoic sedimentary exhalative (SEDEX) mineralization. J. Asian Earth Sci. 57, 54–75.
Guillemette, N., Williams-Jones, A., 1993. Genesis of the Sb–W–Au deposits at Ixtahuacan, Guatemala: evidence from fluid inclusions and stable isotopes. Mineral. Deposita 28, 167–180.
Hagemann, S.G., Lüders, V., 2003. P–T–X conditions of hydrothermal fluids and precipitation mechanism of stibnite-gold mineralization at the Wiluna lode-gold deposits, Western Australia: conventional and infrared microthermometric constraints. Mineral. Deposita 38, 936–952.
Harlov, D.E., 2012. The potential role of fluids during regional granulite-facies dehydration in the lower crust. Geosci. Front. 3 (6), 813–827.
He, J., Ma, D.S., Liu, Y.J., 1996. Geochemistry of mineralization in the Zhazixi antimony ore belt on the margin of the Jiangnan old land. Mineral Deposits 15, 41–52 (in Chinese with English abstract).
Hou, T., Zhang, Z.C., Ye, X.R., Encarnacion, J., Reichow, M.K., 2011. Noble gas isotopic systematics of Fe–Ti–V oxide ore-related mafic–ultramafic layered intrusions in the Panxi area, China: the role of recycled oceanic crust in their petrogenesis. Geochim. Cosmochim. Acta 75, 6727–6741.
Hronsky, J.A., Groves, D.I., Loucks, R.R., Begg, G.C., 2012. A unified model for gold mineralisation in accretionary orogens and implications for regional-scale exploration targeting methods. Mineral. Deposita 47 (4), 339–358.
Hu, R.Z., Bi, X.W., Turner, G., Burnard, P.G., 1997. He–Ar isotopic systematics of fluid inclusions in pyrite from Machangqing copper deposit, Yunnan, China. Sci. China Ser. D. 27, 503–508 (in Chinese).
Hu, R.Z., Burnard, P.G., Turner, G., Bi, X.W., 1998. Helium and Argon isotope systematics in fluid inclusions of Machangqing copper deposit in west Yunnan province, China. Chem. Geol. 146, 55–63.
Hu, R.Z., Bi, X.W., Turner, G., Burnard, P.G., 1999a. He and Ar isotope geochemistry of ore-forming fluid in Ailaoshan gold metallogenic belt. Sci. China Ser. D. 29, 321–330 (in Chinese with English abstract).
Hu, R.Z., Bi, X.W., Turner, G., Burnard, P.G., 1999b. Helium and argon isotope geochemistry of metallogenic fluids of gold deposit belt in Ailaoshan. Sci. China Ser. D. 29, 321–330.
Hu, R.Z., Burnard, P.G., Bi, X.W., Zhou, M.F., Peng, J.T., Su, W.C., Wu, K.X., 2004. Helium and argon isotope geochemistry of alkaline intrusion-associated gold and copper deposits along the Red River-Jinshajiang fault belt, SW China. Chem. Geol. 203, 305–317.
Hunan Bureau of Geology and Mineral Resources (HBGMR), 1988. Regional Geology of Hunan Province. Geological Publishing House, Beijing, pp. 1–719 (in Chinese).
Kendrick, M.A., Burgess, R., Pattrick, R.A.D., Turner, G., 2001. Fluid inclusion noble gas and halogen evidence on the origin of Cu-Porphyry mineralising fluids. Geochim. Cosmochim. Acta 65, 2651–2668.
Kendrick, M.A., Burgess, R., Pattrick, R.A.D., Turner, G., 2002. Hydrothermal fluid origins in a fluorite-rich Mississippi Valley-type district: combined noble gas (He, Ar, Kr) and halogen (Cl, Br, I) analysis of fluid inclusions from the South Pennine ore field, United Kingdom. Econ. Geol. 97, 435–451.
Kendrick, M.A., Scambelluri, M., Honda, M., Phillips, D., 2011. High abundances of noble gas and chlorine delivered to the mantle by serpentinite subduction. Nat. Geosci. 4, 807–812.
Kerrich, R., Goldfarb, R., Groves, D., Garwin, S., Jia, Y.F., 2000. The characteristics, origins, and geodynamic settings of supergiant gold metallogenic provinces. Sci. China Ser. D. 43, 1–68.
Kouzmanov, K., Pettke, T., Heinrich, C.A., 2010. Direct analysis of ore-precipitating fluids: combined IR microscopy and LA-ICP-MS study of fluid inclusions in opaque ore minerals. Econ. Geol. 105, 351–373.
Kucha, H., Raith, J.G., 2009. Gold-oxysulphides in copper deposits of the Greywacke Zone, Austria: a mineral chemical and infrared fluid inclusion study. Ore Geol. Rev. 35 (1), 87–100.
Lamadrid, H.M., Lamb, W.M., Santosh, M., Bodnar, R.J., 2013. Raman spectroscopic characterization of $H_2O$ in $CO_2$-rich fluid inclusions in granulite facies metamorphic rocks. Gondwana Res. 2013, 1–10.
Landis, G.P., Hofstra, A.H., 2012. Ore genesis constraints on the Idaho cobalt belt from fluid inclusion gas, noble gas isotope, and ion ratio analyses. Econ. Geol. 107 (6), 1189–1205.
Lawrence, D.M., Treloar, P.J., Rankin, A.H., Boyce, A., Harbidge, P., 2013. A fluid inclusion and stable isotope study at the Loulo mining district, Mali, West Africa: implications for multifluid sources in the generation of orogenic gold deposits. Econ. Geol. 108 (2), 229–257.
Li, S.J., Liang, J.C., Yi, S.J., 1983. Fold structure and its ore-controlling in the Woxi Au–Sb–W deposit, western Hunan. Hunan Geol. 2 (1), 15–22 (in Chinese).
Li, X.H., Li, W.X., Li, Z.X., Luo, C.H., Wang, J., Ye, M.F., Yang, Y.H., 2009. Amalgamation between the Yangtze and Cathaysia Blocks in South China: constraints from SHRIMP U–Pb zircon ages, geochemistry and Nd–Hf isotopes of the Shuangxiwu volcanic rocks. Precambrian Res. 174, 117–128.
Li, G.L., Hua, R.M., Zhang, W.L., Hu, D.Q., Wei, X.L., Huang, X.E., Xie, L., Yao, J.M., Wang, X.D., 2011. He–Ar isotope composition of pyrite and wolframite in the Tieshanlong tungsten deposit, Jiangxi, China: implications for fluid evolution. Resour. Geol. 61 (4), 356–366.
Liang, B.Y., Zhang, Z.R., 1986. A study on the typomorphic properties of quartz in Woxi Au–Sb–W deposit, western Hunan. Hunan Geol. 5, 17–25 (in Chinese with English abstract).
Liang, J.C., Li, S.J., Y S.J., 1981. A preliminary discussion on micro-textures and fabrics of quartz layers in the Woxi gold deposits in Hunan. J. Guilin Coll. Metall. Geol. 1 (3), 41–52 (in Chinese with English abstract).
Lindaas, S.E., Kulis, J., Campbell, A.R., 2002. Near-infrared observation and microthermometry of pyrite-hosted fluid inclusions. Econ. Geol. 97, 603–618.
Liu, Y.J., 1992. Fold structure of the Woxi gold–antimony–tungsten deposit in west Hunan and its ore-controlling regularity as well as dynamic ore-forming process. Mineral Deposits 11 (2), 134–141 (in Chinese with Engligh abstract).
Liu, X.F., Yuan, S.D., Wang, X.D., Wu, S.H., Yuan, Y.B., 2013. Fluid inclusions and ore genesis of the Jinchuantang tin-bismuth deposit, Hunan province, China. Acta Petrol. Sin. 12, 4245–4260 (in Chinese with English abstract).

Lott, D.A., Coveney, R.M., Murowchick, J.B., Grauch, R.I., 1999. Sedimentary exhalative nickel–molybdenum ores in South China. Econ. Geol. 94, 1051–1066.
Lu, H.Z., Fan, H.R., Ni, P., Ou, G.X., Shen, K., Zhang, W.H., 2004. Fluid Inclusion. Science Press, Beijing (in Chinese).
Lu, H.Z., Wang, Z.G., Wu, X.Y., Zhu, X.Q., Chen, W.Y., Luo, X.L., Hu, R.Z., 2012. Turbidite Hosted Gold Deposits. Science Press, Beijing (in Chinese).
Lüders, V., 1996. Contribution of infrared microscopy to fluid inclusion studies in some opaque minerals (wolframite, stibnite, bournonite): metallogenic implications. Econ. Geol. Bull. Soc. 91, 1462–1468.
Lüders, V., Ziemann, M., 1999. Possibilities and limits of infrared light microthermometry applied to studies of pyrite-hosted fluid inclusions. Chem. Geol. 154, 169–178.
Luo, X.L., Yi, S.J., Liang, J.C., 1984. Ore genesis of the Woxi Au–Sb deposit, western Hunan. Geol. Prospect. 20, 1–10 (in Chinese).
Luque, F.J., Huizenga, J.M., Crespo-Feo, E., Wada, H., Ortega, L., Barrenechea, J.F., 2014. Vein graphite deposits: geological settings, origin, and economic significance. Mineral. Deposita 49 (2), 261–277.
Mao, J.W., Li, H.Y., 1997. Research on genesis of the gold deposits in the Jiangnan Terrain. Geochemica 26, 71–81 (in Chinese with English abstract).
Mao, J.W., Li, Y.Q., Goldfarb, R., He, Y., Zaw, K., 2003. Fluid inclusion and noble gas studies of the Dongping gold deposit, Hebei province, China: a mantle connection for mineralization? Econ. Geol. 98 (3), 517–534.
McCuaig, T.C., Kerrich, R., 1998. P–T–t–deformation–fluid characteristics of lode gold deposits: evidence from alteration systematics. Ore Geol. Rev. 12, 381–453.
Mernagh, T.P., 2001. A fluid inclusion study of the Fosterville mine: a turbidite-hosted gold field in the Western Lachlan Fold Belt, Victoria, Australia. Chem. Geol. 173, 91–106.
Moritz, R., 2006. Fluid salinities obtained by infrared microthennometry of opaque minerals: implications for ore deposit modeling — A note of caution. J. Geochem. Explor. 89, 284–287.
Naden, J., Shepherd, T.J., 1989. Role of methane and carbon dioxide in gold deposition. Nature 342, 793–795.
Nagao, K., Takaoka, N., Matsubayashi, O., 1979. Isotopic anomalies of rare gases in the Nigorikawa geotheramal area, Hokkaido, Japan. Earth Planet. Sci. Lett. 44, 82–90.
Nagao, K., Takaoka, N., Matsubayashi, O., 1981. Rare gas isotopic compositions in natural gases of Japan. Earth Planet. Sci. Lett. 53, 175–188.
Niu, H.C., Ma, D.S., 1991. Fluid inclusions studies of Jiangnan type gold deposits in western Hunan province. Acta Mineral. Sin. 11, 386–394 (in Chinese with English abstract).
Ozima, M., Podosek, F.A., 2002. Noble Gas Geochemistry. Cambridge University Press, Cambridge.
Peng, B., Frei, R., 2004. Nd–Sr–Pb isotopic constraints on metal and fluid sources in W–Sb–Au mineralization at Woxi and Liaojiaping (western Hunan, China). Mineral. Deposita 39, 313–327.
Peng, J.T., Hu, R.Z., Zhao, J.H., Fu, Y.Z., Lin, Y.X., 2003a. Scheelite Sm–Nd dating and quartz Ar–Ar dating for Woxi Au–Sb–W deposit, western Hunan. Chin. Sci. Bull. 48, 2640–2646.
Peng, J.T., Hu, R.Z., Zhao, J.H., Fu, Y.Z., 2003b. The ore-forming fluid with a marked radiogenic $^{87}Sr$ signature from the Woxi Au–Sb–W deposit and its significant implication. Bull. Mineral. Petrol. Geochem. 22, 193–196 (in Chinese with English abstract).
Peng, J.T., Hu, R.Z., Zhao, J.H., Fu, Y.Z., Yuan, S.D., 2005. Rare earth element (REE) geochemistry for scheelite from the Woxi Au–Sb–W deposit, western Hunan. Geochimica 34 (2), 115–122 (in Chinese with English abstract).
Pichavant, M., Ramboz, C., Weisbrod, A., 1982. Fluid immiscibility in natural processes: Use and misuse of fluid inclusion data: I. Phase equilibria analysis — A theoretical and geometrical approach. Chem. Geol. 37, 1–27.
Polito, P.A., Bone, Y., Clarke, J.D.A., Mernagh, T.P., 2001. Compositional zoning of fluid inclusions in the Archaean Junction gold deposit, Western Australia: a process of fluid–wall–rock interaction? Aust. J. Earth Sci. 48 (6), 833–855.
Rai, V.K., Murty, S.V.S., Ott, U., 2003. Noble gases in ureilites: cosmogenic, radiogenic, and trapped components. Geochim. Cosmochim. Acta 67, 4435–4456.
Ramboz, C., Pichavant, M., Weisbrod, A., 1982. Fluid immiscibility in natural processes: use and misuse of fluid inclusion data: II. Interpretation of fluid inclusion data in terms of immiscibility. Chem. Geol. 37, 29–48.
Reynolds, J.H., Hohenberg, C.M., Lewis, R.S., Davis, P.K., Kaiser, W.A., 1970. Isotopic analysis of rare gases from stepwise heating of lunar fines and rocks. Science 167, 545–548.
Ridley, J.R., Diamond, L.W., 2000. Fluid chemistry of orogenic lode gold deposits and implications for genetic models. Rev. Econ. Geol. 13, 141–162.
Robert, F., Kelly, W.C., 1987. Ore-forming fluids in Archean gold-bearing quartz veins at the Sigma mine, Abitibi greenstone belt, Quebec, Canada. Econ. Geol. 82, 1464–1482.
Roedder, E., 1984. Fluid inclusions. Miner. Soc. Am. Rev. Miner. 12, 1–644.
Schaaf, P., MÜller-Sohnius, D., 2002. Strontium and neodymium isotopic study of Libyan desert glass: inherited Pan-African age signatures and new evidence for target material. Meteorit. Planet. Sci. 37, 565–576.
Shao, J.B., Wang, P., Chen, D.Z., 1996. Mineralogical studies on pyrites in Woxi Au–Sb–W deposit, western Hunan. Hunan Geol. 15, 26–33 (in Chinese with English abstract).
Shi, M.K., Fu, B.Q., Jin, X.X., Zhou, X.C., 1993. Antimony Metallogeny in the Central Part of Hunan Province. Hunan Science & Technology Press, Changsha (in Chinese).
Sibson, R.H., Robert, F., Poulsen, K.H., 1988. High-angle reverse faults, fluid-pressure cycling, and mesothermal gold–quartz deposits. Geology 16, 551–555.
Singer, B., Brown, L.L., 2002. The Santa Rosa event: 40Ar/39Ar and paleomagnetic results from the Valles rhyolite near Jaramillo Creek, Jemez Mountains, New Mexico. Earth Planet. Sci. Lett. 197, 51–64.
Stuart, F.M., Turner, G., Duckworth, R.C., Fallick, A.E., 1994. Helium-isotopes as tracers of trapped hydrothermal fluids in ocean-floor sulfides. Geology 22, 823–826.
Sun, X.M., Xiong, D.X., Wang, S.W., Shi, G.Y., Zhai, W., 2006. Noble gases isotopic composition of fluid inclusions in scheelites collected from Daping gold mine, Yunnan province, China, and its application for ore genesis. Acta Petrol. Sin. 22, 725–732 (in Chinese with English abstract).
Sun, X.M., Zhang, Y., Xiong, D.X., Sun, W.D., Shi, G.Y., Zhai, W., Shengwei, Wang, 2009. Crust and mantle contributions to gold-forming process at the Daping deposit, Ailaoshan gold belt, Yunnan, China. Ore Geol. Rev. 36, 235–249.
Tomkins, A.G., 2013. On the source of orogenic gold. Geology 41 (12), 1255–1256.
Tripathi, P., Parthasarathy, G., Ahmad, S.M., Pandey, O.P., 2012. Mantle-derived fluids in the basement of the Deccan trap: evidence from stable carbon and oxygen isotopes of carbonates from the Killari borehole basement, Maharashtra, India. Int. J. Earth Sci. 101 (5), 1385–1395.
Van den Kerkhof, A.M., Hein, U.F., 2001. Fluid inclusion petrography. Lithos 55, 27–47.
Wang, X.D., Ni, P., Yuan, S.D., Wu, S.H., 2013. Fluid inclusion studies on coexisting cassiterite and quartz from the Piaotang tungsten deposit, Jiangxi province, China. Acta Geol. Sin. 87 (6), 850–859 (in Chinese with English abstract).
Wei, W.F., Hu, R.Z., Bi, X.W., Peng, J.T., Su, W.C., Song, S.Q., Shi, S.H., 2012. Infrared microthermometric and stable isotopic study of fluid inclusions in wolframite at the Xihuashan tungsten deposit, Jiangxi province, China. Mineral. Deposita 47, 589–605.
Wieler, R., Baur, H., Signer, P., 1986. Noble gases from solar energetic particles revealed by closed system stepwise etching of lunar soil minerals. Geochim. Cosmochim. Acta 50, 1997–2017.
Wilkinson, J.J., 2001. Fluid inclusions in hydrothermal ore deposits. Lithos 55, 229–272.
Xu, S., Zheng, G.D., Nakai, S.I., Wakita, H., Wang, X.B., Guo, Z.F., 2013. Hydrothermal He and $CO_2$ at Wudalianchi intra-plate volcano, NE China. J. Asian Earth Sci. 62, 526–530.
Yang, X., 1992. Source of ore material and paragenesis of orebuilding elements in Woxi Au–Sb–W deposit, Hunan. J. Chengdu Coll. Geol. 19, 23–31 (in Chinese with English abstract).
Yang, Y.F., Li, N., Chen, Y.J., 2012. Fluid inclusion study of the Nannihu giant porphyry Mo–W deposit, Henan province, China: implications for the nature of porphyry ore-fluid systems formed in a continental collision setting. Ore Geol. Rev. 46, 83–94.
Yang, Y.F., Chen, Y.J., Li, N., Mi, M., Xu, Y.L., Li, F.L., Wan, S.Q., 2013. Fluid inclusion and isotope geochemistry of the Qian'echong giant porphyry Mo deposit, Dabie Shan, China: a case of NaCl-poor, $CO_2$-rich fluid systems. J. Geochem. Explor. 124, 1–13.
Yao, Z.K., Zhu, R.B., 1993. Polygenetic compound model for the Fuzhuxi gold deposit of Hunan province and its prospecting. Geotecton. Metallog. 17, 199–209 (in Chinese with English abstract).
Ye, X.R., Tao, M.X., Yu, C.N., Zhang, M.J., 2007. Helium and neon isotopic compositions in the ophiolites from the Yarlung Zangbo River, Southwestern China: the information from deep mantle. Sci. China Ser. D Earth Sci. 50, 801–812.
Yokart, B., Barr, S.M., Williams-Jones, A.E., Macdonald, A.S., 2003. Late-stage alteration and tin-tungsten mineralization in the Khuntan Batholith, northern Thailand. J. Asian Earth Sci. 21, 999–1018.
Yu, D.L., 1997. A study on the geological and geochemical characteristics of bake gold deposit, east Guizhou. Geol. Geochem. 12–17 (in Chinese with English abstract).
Zachariáš, J., Žák, K., Pudilová, M., Snee, L.W., 2013. Multiple fluid sources/pathways and severe thermal gradients during formation of the Jílové orogenic gold deposit, Bohemian Massif, Czech Republic. Ore Geol. Rev. 54, 81–109.
Zeng, Q.D., Wang, Z.C., He, H.Y., Wang, Y.B., Zhang, S., Liu, J.M., 2014. Multiple isotope composition (S, Pb, H, O, He, and Ar) and genetic implications for gold deposits in the Jiapigou gold belt, Northeast China. Mineral. Deposita 49 (1), 145–164.
Zhai, W., Sun, X.M., Wu, Y.S., Sun, Y.Y., Hua, R.M., Ye, X.R., 2012. He–Ar isotope geochemistry of the Yaoling-Meiziwo tungsten deposit, North Guangdong province: constraints on Yanshanian crust-mantle interaction and metallogenesis in SE China. Chin. Sci. Bull. 57, 1137–1146 (in Chinese with English abstract).
Zhang, L.G., 1985. Stable isotope geological study on the W–Sb–Au deposit in the upwarped district, Xuefengshan, western Hunan. Geol. Prospect. 21, 24–28 (in Chinese).
Zhang, Z.R., Yang, S.X., Chen, M.X., 1996. A study on the mineralogy of the Woxi Au–Sb–W deposit in Hunan. In: Xianlin, Luo, Dongqiu, Zhong, Gaosheng, Li (Eds.), Geology of Woxi-type Stratabound Gold Deposit in Hunan Province. Seismological Press, Beijing, pp. 216–232 (in Chinese).
Zhang, L., Chen, H.Y., Chen, Y.J., Qin, Y.J., Liu, C.F., Zheng, Y., Jansen, N.H., 2012. Geology and fluid evolution of the Wangfeng orogenic-type gold deposit, Western Tian Shan, China. Ore Geol. Rev. 49, 85–95.
Zhang, G.W., Guo, A.L., Wang, Y.J., Li, S.Z., Dong, Y.P., Liu, S.F., He, D.F., Cheng, S.Y., Lu, R.K., Yao, A.P., 2013. Tectonics of South China continent and its implications. Sci. China: Earth Sci. 56, 1804–1838.
Zhou, T.H., Goldfarb, R.J., Phillips, N.I, 2002. Tectonics and distribution of gold deposits in China—an overview. Mineral. Deposita 37, 249–282.
Zhu, M.T., Zhang, L.C., Wu, G., He, H.Y., Cui, M.L., 2013. Fluid inclusions and He–Ar isotopes in pyrite from the Yinjiagou deposit in the southern margin of the North China Craton: a mantle connection for poly-metallic mineralization. Chem. Geol. 351, 1–14.
Zhu, Y.N., Peng, J.T., Liu, S.Y., Sun, Y.Z., 2014. Mineral deposit geology and trace element geochemistry of wolframite from the Woxi deposit, western Hunan, China. Geochimica 43 (3), 287–300 (in Chinese with English abstract).